Molecular basis for control of diverse genome stability factors by the multi-BRCT scaffold Rtt107

Bingbing Wan[1], **Jian Wu**[2], **Xiangzhou Meng**[1], **Ming Lei**[2,3,4,5,*], **Xiaolan Zhao**[1,6,*]

[1]Molecular Biology Department, Memorial Sloan Kettering Cancer Center, New York, NY 10065, USA

[2-3]Shanghai Institute of Precision Medicine, and Key laboratory of Cell Differentiation and Apoptosis of Chinese Ministry of Education, Shanghai Jiao Tong University School of Medicine, 200125 Shanghai, China

[4]National Facility for Protein Science in Shanghai, Zhangjiang Lab, Shanghai, 201210, China

[5]Shanghai Science Research Center, Chinese Academy of Sciences, Shanghai, 201204, China

[6]Lead Contact

SUMMARY

BRCT domains support a myriad of protein-protein interactions involved in genome maintenance. While di-BRCT recognition of phospho-proteins is well-known to support the genotoxic response, whether multi-BRCT domains can acquire distinct structures and functions are unclear. Here we present the tetra-BRCT structures from the conserved yeast protein Rtt107 in free and ligand-bound forms. The four BRCT repeats fold into a tetrahedral arrangement and specifically recognize unmodified ligands using a bi-partite binding mechanim, suggesting 'repeat origami' enabling function acquisition. Functional studies show that Rtt107 binding of partner proteins of diverse activities promotes genome replication and stability in both distinct and concerted manners. A unified theme is that tetra- and di-BRCT domains of Rtt107 collaborate to recruit partner proteins to chromatin. Our work thus illustrates how a master regulator uses two types of BRCT domains to recognize distinct genome factors and direct them to chromatin for constitutive genome protection.

Graphical Abstract

Rtt107

tetra-BRCT

Smc5/6

Recognition Sequence
('zip code')

Mms22

Slx4

Others

di-BRCT

P

γH2A zone

**Constitutively Promote Genome
Duplication and Stability**

eTOC Blurb

Di-BRCT domains recognize phospho-proteins and contribute to the DNA damage response. Wan et al. show that a distinct architecture formed by four BRCTs of the Rtt107 protein enables recognition of phospho-free ligands and supports constitutive genome protection. This work uncovers structural plasticity and functional diversity of BRCT domains.

Keywords

Genome maintenance factors; BRCT domains; protein network; hub protein; Rtt107; Smc5/6; Mms22; Slx4; rDNA

INTRODUCTION

Genome maintenance requires a collaborative network of proteins with roles in chromatin replication, repair, and segregation. The architecture of this vast network relies on protein-binding domains that support specific interactions. BRCT (BRCA1 C-Terminal) domains, initially identified in the tumor suppressor protein BRCA1, are key constituents of the genome maintenance network across species and support hundreds of protein interactions in human cells (Koonin et al., 1996; Woods et al., 2012). Di-BRCT domains comprising two adjacent BRCT repeats can recognize phosphorylated proteins, thereby establishing situation-specific protein interactions critical for the DNA damage response (Manke et al., 2003; Yu et al., 2003). The importance of di-BRCT binding to phospho-peptides is

highlighted by its essential role in BRCA1-mediated tumor suppression (Shakya et al., 2011). An open question regarding the underlying principles of BRCT-based networks is whether multi-BRCT domains act as an assembly of di-BRCTs or have unique functions.

To address this question, we investigated the conserved six-BRCT domain-containing Rtt107 protein from budding yeast (Rouse, 2004) (Figure 1A). The most C-terminal two BRCTs (BRCT5-6) of Rtt107 and its homologs, including the fission yeast Brc1 and human PTIP, adopt a canonical di-BRCT fold and bind to γH2A, a phosphorylated form of histone H2A associated with DNA damage and replication sites (Li et al., 2012; Manke et al., 2003; Williams et al., 2010; Yan et al., 2011; Yu et al., 2003). Consistent with this interaction, Rtt107, Brc1, and PTIP promote the DNA damage response (Jowsey et al., 2004; Rouse, 2004; Sheedy et al., 2005). The structures of the four other BRCTs (BRCT1-4) of these proteins and their functional interplay with the corresponding BRCT5-6 domains are unclear. As protein interactions underlie the roles of Rtt107 family of factors, addressing these questions is of mechanistic significance.

The Rtt107 region containing BRCT1-4 interacts with the Nse6 subunit of the Smc5/6 complex, the Mms22 subunit of the Cul8 ubiquitin ligase, and the Slx4 protein (Chin et al., 2006; Leung et al., 2011; Roberts et al., 2006; Zappulla et al., 2006). Like Rtt107, these interactors are conserved, and mutations of their human homologs cause DNA fragility with some leading to genome instability syndromes (Duro et al., 2010; Kim et al., 2011; O'Donnell et al., 2010; van der Crabben et al., 2016). While members of this Rtt107 interactome promote survival upon exposure to genotoxins via multiple means (Duro et al., 2008; Hang et al., 2015; Ohouo et al., 2013), how Rtt107 interactions affect genome maintenance during normal growth is unclear. Addressing this question will shed important light on Rtt107 interactome functions in continuous genome protection and their human homologs' involvement in diseases.

Here, we present high-resolution structures of the Rtt107 BRCT1-4 domains with and without bound ligand peptides. These structures reveal unique BRCT repeat origami and molecular basis for recognizing half a dozen unmodified ligands. Cell-based studies uncover a continuous requirement for the Rtt107-client interactions in genome protection, and the collaborative nature of its tetra- and di-BRCT domains in targeting client proteins to chromatin. These findings provide structural and molecular bases for how the Rtt107 master regulator recognizes specific genome stability factors and directs them to chromatin for continuous genome protection.

RESULTS

The N-terminal four BRCT repeats of Rtt107 form a compact tetrahedral architecture

To understand the functional mechanisms of Rtt107 and its interaction network, we first determined the structure of the BRCT1-4 domains of Rtt107 (Rtt107$_{NTD}$) at a resolution of 2.3 Å (Figures 1B and S1A-S1B; Table 1). Different from a predicted tandem array of di-BRCTs, Rtt107$_{NTD}$ forms a compact tetrahedral architecture, with individual BRCT units packing into the four apexes of a tetrahedron (Figures 1B and S1C-S1D). This intriguing 'repeat origami' is enabled by three features. First, in contrast to the parallel repeat

arrangement in di-BRCTs (Clapperton et al., 2004; Shiozaki et al., 2004; Williams et al., 2004), adjacent BRCTs within the tetra-BRCT are rotated relative to each other (Figure S1E). Such an out-of-register repeat configuration makes a higher-order folding feasible. Second, inter-BRCT linkers play much more prominent roles in forming the inter-repeat interfaces than linkers in di-BRCTs (Figures S1D and S1F). Such a linker-interface provides more freedom in repeat arrangement. Third, BRCT repeats not adjacent in primary sequence also make extensive contacts in $Rtt107_{NTD}$ (Figure S1G). Collectively, these unique features drive the entire $Rtt107_{NTD}$ region to fold into a tight tetrahedral architecture.

It is known that di-BRCT binding to phospho-Ser/Thr depends on a conserved basic site in the first BRCT that consists of a serine or a threonine between $\beta 1$ and $\alpha 1$ followed by a glycine, and a lysine in $\alpha 2$ (Clapperton et al., 2004; Shiozaki et al., 2004; Williams et al., 2004). This site is absent in BRCT1-3 of Rtt107: the equivalent positions of S/T and K are occupied by buried hydrophobic residues and glycine is replaced by alanine or serine (Figure S1D). BRCT4 of Rtt107 does possess T385 and K426 fitting to a phospho-peptide binding motif, but glycine is replaced by asparagine (Figure S1D). Thus, the four BRCT units in $Rtt107_{NTD}$ do not contain phospho-peptide binding sites as seen in classical di-BRCT domains. Interestingly, a panel of seven positively charged residues in BRCT1 (R107, H108, R110), BRCT2 (R160), and BRCT4 (R392, K425, K426) form a deep and large-sized highly basic pocket (Figures 1C, S1D, and S1H). We hypothesized that this prominent feature may contribute to Rtt107 tetra-BRCT interactions via a different mechanism. For simplicity, this deep and basic pocket formed by Rtt107 BRCT1, –2 and –4 is referred to as RBIP (Rtt107 tetra-BRCT basic interaction pocket) hereafter.

Rtt107 tetra-BRCT recognizes multiple unphosphorylated peptides

To elucidate how the Rtt107 tetra-BRCT domain recognizes genome maintenance factors, including Nse6, Mms22, and Slx4, we first mapped their interaction regions using the yeast two-hybrid (Y2H) assay. Short N-terminal fragments of Nse6 (residues 2-46) and Mms22 (residue 2-38) were found to be necessary and sufficient for $Rtt107_{NTD}$ interactions (Figures S2A and S2B). Intriguingly, Slx4 contains two non-overlapping fragments (residues 407-445 and 535-587) that interacted independently with $Rtt107_{NTD}$ (Figure S2C). We refer to $Nse6_{2-46}$ and $Mms22_{2-38}$ as the Rtt107-interaction motif (RIM) containing regions, or $Nse6_{RIM}$ and $Mms22_{RIM}$, respectively. Similarly, $Slx4_{407-445}$ and $Slx4_{535-587}$ are referred to as $Slx4_{RIM1}$ and $Slx4_{RIM2}$, respectively. The four RIM peptides share no sequence homology and are predicted to be unstructured (Figures S2A-S2C). *In vitro*, purified RIM-containing peptides bound to $Rtt107_{NTD}$ with an affinity ranging from 15 nM in the case of $Mms22_{RIM}$ to 34 μM for $Slx4_{RIM1}$, as measured by isothermal titration calorimetry (ITC) (Figures 1D and S2D). We conclude that Rtt107 tetra-BRCT binds to Nse6, Mms22, or Slx4 via one or two peptides in the absence of phosphorylation and with wide range affinities. To understand how Rtt107 tetra-BRCT recognizes these diverse peptides with different affinities, we proceeded to obtain crystal structures of the different complexes.

The structure of the $Rtt107_{NTD}$–$Nse6_{RIM}$ complex reveals a bipartite interface

We first determined the $Rtt107_{NTD}$–$Nse6_{RIM}$ complex structure of at a 2.4 Å resolution (Table 1). $Rtt107_{NTD}$ exhibited essentially the same conformation as seen in the ligand-free

state (Figure 2A). The electron density map showed that residues 13-19 and 23-41 of Nse6 assumed a well-defined conformation whereas the linker (residues 20-22) only exhibited clear density for the main chain atoms (Figures 2A, S3A-S3B). Accordingly, the Rtt107$_{NTD}$–Nse6$_{RIM}$ interaction entails a bipartite binding mode with two distinct interfaces, burying 460 and 770 Å^2 of surface, respectively.

The N-terminal region of Nse6$_{RIM}$ (residues 13-19, Nse6$_{RIM-N}$) packs along one side of BRCT4 of Rtt107 through main chain hydrogen-bonding interactions and points into the RBIP region that we hypothesized as a potential protein interaction site (Figure 2B). At the bottom of this pocket, residues DSQ$_{17-19}$ of Nse6 mediate an extensive electrostatic network with Rtt107$_{NTD}$: the side chain of D17 forms two salt bridges with Rtt107^{R110} and Rtt107^{R392}, while the S18 side chain forms a hydrogen bond with Rtt107^{K426} and the Q19 side chain coordinates two hydrogen bonds with Rtt107^{R110} and Rtt107^{Y387} (Figure 2C).

In contrast to Nse6$_{RIM-N}$, the C-terminal region of Nse6$_{RIM}$ (residues 23-41, Nse6$_{RIM-C}$) adopts an extended conformation meandering along a shallow hydrophobic groove between BRCT2 and –4 of Rtt107 (Figure 2B). Near the C-terminal end of Nse6$_{RIM-C}$, the F36 side chain is embedded in a hydrophobic pocket formed by Rtt107$^{K131, K136, Y139}$ (Figure 2D). Additionally, multiple main chain hydrogen-bonding interactions strengthen the Nse6$_{RIM-C}$–Rtt107$_{NTD}$ interface (Figure 2E). Together, these elaborate interactions extend the contact interface and contribute to the specific recognition of the Nse6$_{RIM}$ peptide by Rtt107$_{NTD}$.

Consistent with our structural data, Y2H assays showed that individual alanine substitutions of Nse6$_{RIM-N}$ residues D17, S18, and Q19, which constitute an electrostatic interface with Rtt107$_{NTD}$, abolished or greatly reduced Y2H interactions with Rtt107 (Figure 2F). In addition, mutations of Nse6$_{RiM-C}$ residues that contribute to the hydrophobic contacts with Rtt107$_{NTD}$ reduced the interaction, with F36R showing the strongest defect (Figure 2F). These data support that Rtt107$_{NTD}$ associates with Nse6$_{RIM}$ using a bipartite recognition mechanism, with electrostatic contact of Nse6$_{RIM-N}$ being more critical than the hydrophobic contact of Nse6$_{RIM-C}$.

We next examined the consequences of alanine substitution of the Nse6 DSQ$_{17-19}$ motif (referred to as Nse6^{RIM}) in the context of the endogenously expressed full-length protein. Nse6^{RIM} maintained its association with Nse2, another subunit of the Smc5/6 complex, but failed to interact with Rtt107 in co-immunoprecipitation experiments (Figure 2G). Hence, the observed electrostatic interface between Nse6 and Rtt107 is necessary for their interaction *in vitro* and *in vivo*.

The Rtt107$_{NTD}$–Mms22$_{RIM}$ interaction also uses a bipartite mode but has distinct features

We moved on to examine Mms22$_{RIM}$. Guided by our structural understanding of Nse6$_{RIM}$, we found that Mms22$_{RIM}$ shares an uneven distribution of amino acids as seen in Nse6$_{RIM}$, including a highly acidic N-terminal half and a hydrophobic C-terminal half (Figures S4A and S4B). This raised the possibility that Mms22$_{RIM}$ might use a bipartite mode to interact with Rtt107$_{NTD}$ similar to Nse6$_{RIM}$. To test this premise, we solved Rtt107$_{NTD}$–Mms22$_{RIM}$ complex structure (Figure 3A; Table 1). Remarkably, the C-terminal hydrophobic region of

Mms22$_{RIM}$ (Mms22$_{RIM-C}$, residues 22-37) binds to the same hydrophobic groove between BRCT2 and –4 of Rtt107$_{NTD}$ as Nse6$_{RIM-C}$ (Figures 3B; S3C-S3D).

Despite the overall similarity, the local landscapes of the Rtt107$_{NTD}$ hydrophobic groove in the two complexes are substantially different (Figure 3C). In the Rtt107$_{NTD}$–Nse6$_{RIM}$ complex, the side chains of Rtt107$^{K136, K373}$ protrude into the central space as a crossbeam in the groove, forming part of the hydrophobic pocket for F36 of Nse6 and forcing the Nse6$_{RIM}$ C-terminus towards BRCT2 of Rtt107 (Figure 3C, top). In contrast, side chains of Rtt107$^{K136, K373}$ in the Rtt107$_{NTD}$–Mms22$_{RIM}$ interface rotate away from the groove, resulting in an enlarged hydrophobic cavity to accommodate side chains of L34 and W35 of Mms22 (Figure 3C, bottom). Notably, the side chain of Y33 of Mms22 occupies the same hydrophobic pocket as F36 of Nse6, although in an opposite orientation and forming more extensive interactions with Rtt107 (Figures 3C and 3D). As a consequence of this local rearrangement, the interface in the Rtt107$_{NTD}$–Mms22$_{RIM-C}$ complex is extended to 920 Å^2 from 770 Å^2 in the Rtt107$_{NTD}$–Nse6$_{RIM-C}$ complex, explaining the stronger binding affinity of Mms22$_{RIM}$ toward Rtt107$_{NTD}$ (Figure 1D).

Although the acidic N-terminal region of Mms22$_{RIM}$ (Mms22$_{RIM-N}$) is not visible in the electron density map, its proximity to RBIP and their oppositely charged natures suggest that these two regions are closely associated. We used mutagenesis analyses to test this premise. Y2H data showed that like Mms22$_{RIM-C}$, Mms22$_{RIM-N}$ was necessary for Rtt107 binding (Figure S3B). Moreover, point mutations of DSE$_{13-15}$, which resembles the Nse6$_{RIM-N}$ DSQ$_{17-19}$ motif that contacts RBIP (Figures S4A and S4B), reduced the Y2H Rtt107$_{NTD}$ interaction, with the D13 mutations having the strongest effects (Figure 3E). A reduction in interaction was also observed upon mutating the Mms22$_{RIM-C}$ hydrophobic contacts with Rtt107$_{NTD}$ (Figure 3E). Only when D13A was combined with Y33A, L34A, or W35A, Rtt107$_{NTD}$ interaction was abolished (Figure 3E). This result suggests that electrostatic and hydrophobic contacts are both important for the Rtt107–Mms22 interaction, differentiating this interaction from that of Rtt107 and Nse6. Testing one of the combined Mms22 mutations, D13A/Y33A (*mms22^{RIM}*), in the context of the endogenously expressed full-length protein, showed that its association with Rtt107, but not with the Mms1 subunit of the Cul8 ubiquitin E3 complex, was disrupted (Figure 3F). Thus, we conclude that Mms22 also uses a bipartite mode to interact with Rtt107$_{NTD}$, analogously to Nse6; however, the relative contributions by the acidic vs. hydrophobic sequences of their RIMs are different.

Shared and unique features of Rtt107 interaction with Slx4$_{RIM1}$ and Slx4$_{RIM2}$

Our findings that the Rtt107 tetra-BRCT domain recognizes Nse6 and Mms22 RIMs using a similar bipartite mode raised the possibility that this may be a general principle for ligand recognition by this tetra-BRCT. To test this hypothesis, we examined the Slx4 RIMs. The Slx4$_{RIM1}$ sequence has a bipartite structure similar to Nse6$_{RIM}$ and Mms22$_{RIM}$ (Figure S4C). While Slx4$_{RIM1-N}$ contains a DTT$_{422-424}$ motif mimicking the DSE/Q motif in Nse6$_{RIM-N}$ and Mms22$_{RIM-N}$, Slx4$_{RIM1-C}$ contains a stretch of hydrophobic residues similar to Nse6$_{RIM-C}$ and Mms22$_{RIM-C}$ (Figures S4A-S4C). Importantly, as seen for Nse6$_{RIM}$, mutation of the DTT$_{422-424}$ motif abolished the Y2H interaction with Rtt107, while mutation

of hydrophobic residues partially reduced the interaction (Figure 4A). These data suggest that Slx4$_{RIM1}$ also uses a bipartite mode for associating with Rtt107$_{NTD}$, but it resembles Nse6$_{RIM}$ more than Mms22$_{RIM}$ in that the D-S/T-Q/E/T motif makes a major contribution to the interaction.

Slx4$_{RIM2}$ does not have a bipartite sequence as seen in the other three RIMs, but rather contains a stretch of acidic residues in its C-terminal region (Figure S4C). To understand how Slx4$_{RIM2}$ is recognized by Rtt107$_{NTD}$, we determined Rtt107$_{NTD}$–Slx4$_{RIM2}$ complex structure (Figure 4B; Table 1). Unlike the extended conformations of the other RIMs, Slx4$_{RIM2}$ forms a compact fold with a three-stranded β-sheet covered by a short α-helix (Figures 4B; S3E-S3F). Remarkably, this structure sits right on top of the hydrophobic groove between Rtt107's BRCT2 and –4 repeats, which also binds Nse6$_{RIM-C}$ and Mms22$_{RIM-C}$ (Figure 4C). Several Slx4$_{RIM2}$ residues, including I538, V540, L550, and L554, show hydrophobic interactions with Rtt107 in this grove (Figure 4C). Consistently, mutating these residues weakened the Y2H interaction with Rtt107$_{NTD}$ (Figure 4D). Compared with the interfaces in the Rtt107$_{NTD}$–Nse6$_{RIM-C}$ and Rtt107$_{NTD}$–Mms22$_{RIM-C}$ complexes, Slx4$_{RIM2}$ partially occupies the hydrophobic groove of Rtt107$_{NTD}$, with only a 540 Å^2 interface area between Rtt107$_{NTD}$ and Slx4$_{RIM2}$.

Intriguingly, the acidic stretch in the Slx4$_{RIM2}$ C-terminal region is within an extended loop between strands β2 and β3 and fits right into RBIP (Figure 4C). This interface entails an extensive hydrogen-bonding network, with S567, E569, E571, and T572 of Slx4 forming multiple contacts with Rtt107$^{K107, Q126, R160}$ (Figure 4E). Further, S567 of Slx4 coordinates this network by forming intramolecular interactions with E569 and T572 (Figure 4E). Adjacent to this, D566 and E568 of Slx4 form electrostatic interactions with Rtt107^{K426} and Rtt107^{R392}, respectively (Figure 4E). Such an extensive electrostatic network likely compensates for the relatively smaller hydrophobic interface between Slx4$_{RIM2}$ and Rtt107 to support a stable interaction. Notably, the DSE$_{566-568}$ motif within the Slx4 acidic loop fits the D-S/T-Q/E/T consensus in other RIM-N peptides examined. Consistent with a key structural role, the S567A mutation of Slx4 abolished Y2H interaction with Rtt107$_{NTD}$, while D566R and E568R reduced this interaction (Figure 4D). We thus conclude that Slx4$_{RIM2}$ adopts a different conformation from Nse6$_{RIM}$ and Mms22$_{RIM}$, but still associates with Rtt107$_{NTD}$ via the same bipartite mechanism.

To generate a *slx4* mutant that abolishes Rtt107 association, we tested T423A/T424A in Slx4$_{RIM1}$ and S567A in Slx4$_{RIM2}$, which individually exhibited strong Rtt107$_{NTD}$ interaction defects (Figures 4A and 4D). In cells, Slx4-S567A showed more severe defects in Rtt107 association than Slx4-T423A/T424A, and their combined mutation (referred to as *slx4^{RIM}*) completely abolished the Rtt107-Slx4 interaction (Figure 4F). This effect is specific as *slx4^{RIM}* did not change the interactions with another known interactor, Slx1 (Figure 4F).

Mutually exclusive RIM binding of Rtt107$_{NTD}$

Our conclusion that Rtt107 tetra-BRCT uses similar mechanisms to recognize different RIM sequences suggests mutually exclusive interactions. A prediction is that RIM peptides compete with each other for Rtt107 binding. Our *in vitro* competition assay results

supported this prediction. Briefly, the GST-Slx4$_{RIM2}$–Rtt107$_{NTD}$ complex was challenged by a competitor RIM peptide at two-fold molar excess, and the remaining bead-bound complex was examined (Figure S5A). Compared with a control reaction to which no competitor was added, bead-bound Rtt107$_{NTD}$ levels were greatly reduced by the addition of Mms22$_{RIM}$ and moderately by Nse6$_{RIM}$ (Figures 4G and S5B). The different effects are in line with that Mms22$_{RIM}$ has a stronger affinity for Rtt107$_{NTD}$ compared to Nse6$_{RIM}$ and Slx4$_{RIM2}$ (Figure 1D). Less Rtt107$_{NTD}$ was released from GST-Slx4$_{RIM2}$ upon addition of Slx4$_{RIM1}$, compared with Mms22$_{RIM}$ and Nse6$_{RIM}$; however, this was improved when Slx4$_{RIM1}$ was added five-fold in excess (Figures 4H and S5C). In reciprocal experiments, Slx4$_{RIM2}$ effectively released Rtt107$_{NTD}$ bound to GST-Slx4$_{RIM1}$ (Figures 4H and S5C). These results agree with our data that Slx4$_{RIM2}$ binds more strongly to Rtt107$_{NTD}$ than Slx4$_{RIM1}$ and they ocupy the same sites on Rtt107$_{NTD}$. Data above provided biochemical validation of the conclusion that Rtt107$_{NTD}$ recognizes different RIM sequences by similar mechanisms.

Additional RIM-containing proteins expand the scope of the Rtt107 tetra-BRCT interactome

Identification of RIM consensus sequences above enabled us to examine the scope of RIM-mediated Rtt107 interactions in the proteome. We used the most conserved feature of the RIMs, namely the D-S/T-Q/E/T motif present in an acidic loop, to examine reported Rtt107 Y2H interactors (Chin et al., 2006; Princz et al., 2017). We identified DSE$_{187-189}$ in the centromeric protein Scm3, DSN$_{385-387}$ in the homologous recombination protein Rad55, and EST$_{482-484}$ in the Cdc7 kinase, all in unstructured acidic regions (Figure S5D). Significantly, a peptide containing this motif from each of these proteins bound to Rtt107 *in vitro* (Figure S5E). These peptides also interacted with Rtt107$_{NTD}$ in Y2H analysis in a manner dependent on the basic residues of RBIP, as in the case for Nse6$_{RIM}$ and Slx4$_{RIM1}$ (Figure S5F). In addition, these Y2H interactions required the D-S/T-Q/E/T motif of Scm3 Rad55 and Cdc7 (Figure S5G). These data suggest that these three proteins interact with Rtt107 using a similar mechanism as Nse6, Slx4, and Mms22, highlighting the prominent role of the D/E-S/T-Q/E/T/N motif for mediating Rtt107 tetra-BRCT association with partner proteins.

RIM mutants are separation-of-function alleles that lead to genomic instability during growth

After establishing the structural basis of Rtt107 tetra-BRCT interactions with client proteins, we addressed the functional significance of these interactions. Rtt107 associates separately with Nse6, Mms22, and Slx4 during growth and after DNA damage (Hang et al., 2015). However, it has been difficult to pinpoint the roles of these interactions in genome protection, particularly during growth as their null or hypomorphic alleles exhibit pleiotropic defects (Aragon, 2018; Cussiol et al., 2017; Duro et al., 2008; Wan et al., 2016). Because *RIM* mutants (*nse6^{RIM}*, *mms22^{RIM}*, and *slx4^{RIM}*) described above disrupted the associations of their corresponding proteins with Rtt107 but not with other interactors, they likely specifically abolish the functions mediated by interactions with Rtt107. This notion was validated genetically as *RIM* mutants did not worsen the growth nor genotoxin sensitivity of *rtt107Δ* cells, unlike *mms22Δ*, *slx4Δ*, or *smc6-P4* hypomorphic allele (Smc5/6 is essential) (Figure 5A). Based on our biochemical and genetic data, we conclude that *RIM* mutants are separation-of-function alleles uniquely able to reveal the consequences of disrupting the

Rtt107 tetra-BRCT interactions with its client proteins. We note that combining the *RIM* mutations of Slx4, Mms22 and Nse6 conferred less genotoxin sensitivity than *rtt107* (Figure S6A). This finding is consistent with our data that the tetra-BRCT of Rtt107 also interacts with other proteins that contribute to genome protection as decribed above.

We used gross chromosomal rearrangements (GCRs) assay (Putnam et al., 2009) to inquire the effects of *RIM* mutants on overall genome stability during growth. We found that $nse6^{RIM}$, $mms22^{RIM}$, and $slx4^{RIM}$ mutants exhibited 3- to 34-fold increased rates over wild-type levels, while *rtt107* exhibited an even higher rate (Figure 5B). Thus, Rtt107 interactions with Nse6, Mms22, and Slx4 suppress genome instability during continuous growth to different degrees.

Different *RIM* mutants are synthetic sick with unique genome stability mutants

To further understand how *RIM* mutants affect genomic stability, we asked whether they had unique genetic interactor(s). A targeted screen among mutants reported to show negetiave genetic interactions with *rtt107* or mutants of the Smc5/6 complex, Mms22, and Slx4, found that each *RIM* mutant was synthetically sick with the loss of a specific genome stability factor (Figures 5C and 5D). These include the Sgs1 and Rrm3 DNA helicases and the Esc2 structural protein with roles in DNA replication and repair. In contrast to *RIM* mutants, the null or hypomorphic alleles of Mms22, Slx4 or the Smc5/6 complex showed negative interactions with all three tester mutants (Figures S6B-S6D). The *RIM* genetic interactions were also verified by cell doubling time measurements (Figure 5E). In GCR tests, the double mutants of $nse6^{RIM} esc2$, $mms22^{RIM} rrm3$, and $slx4^{RIM} sgs1$ exhibited a further increase in the rates of *RIM* mutants, up to ~850-fold over wild-type levels (Figure 5B). These genetic findings suggest that the functions of Rtt107 binding to distinct client proteins are related to their corresponding genetic interactors.

Rtt107 binding of client proteins supports chromosome replication and rDNA stability

Increased GCR levels and the genetic interactors of *RIM* mutants described above can be both linked to DNA replication(Putnam et al., 2009). We thus tested whether *RIM* mutants impair replication by assessing the duplication of chromosome 12, which provides a sensitive indicator for replication defects due to its containing of the difficult-to-replicate ribosome DNA (rDNA). We used pulsed field gel electrophoresis (PFGE) that allows fully replicated chromosomes to enter the gel but traps partially replicated chromosomes in the gel wells. We found that $nse6^{RIM}$, $mms22^{RIM}$, and $slx4^{RIM}$ mutants were each defective in replicating chromosome 12 in S phase, and *rtt107* cells exhibited a more severe defect, likely reflecting the combined loss of all three interactions (Figure 6A). Moreover, deletion of the buffering gene *SGS1* exacerbated $slx4^{RIM}$ defects (Figure 6A). These results indicate that Rtt107 tetra-BRCT interactions with Nse6, Mms22, and Slx4 promote DNA replication.

We extended this analysis by examining the stability of the rDNA region on chromosome 12. The loss rates of an *ADE2-CAN1* cassette inserted in the rDNA array increased several-fold in $nse6^{RIM}$, $mms22^{RIM}$, or $slx4^{RIM}$ mutants compared with wild-type cells (Figure 6B). Moreover, these defects were enhanced when the buffering gene for each *RIM* mutant was deleted, such that combined mutants exhibited up to ~ 100-fold increase of rDNA marker

loss over wild-type (Figure 6B). Thus, the RIM-dependent Rtt107 interactions protect rDNA stability.

Rtt107 tetra- and di-BRCT domains cooperatively target client proteins to chromatin

Our data so far suggest that though the different Rtt107 interactions have distinct roles, they all contribute to genome replication and stability during growth. This raises the possibility for a unified theme underpinning their genomic effects. As the Rtt107 BRCT5-6 recognizes γH2A that marks replicating chromatin during growth (Li et al., 2012; Szilard et al., 2010), we hypothesized that the Rtt107 tetra-BRCT domain might collaborate with this di-BRCT to recruit the various interacting proteins to chromatin. This model predicts that disrupting the interactions of tetra-BRCT and client proteins or that of di-BRCT and γH2A should both reduce chromatin-bound client protein levels. This was indeed the case for Nse6^{RIM}, Mms22^{RIM}, and Slx4^{RIM} mutant proteins (Figures 6C-6E). In addition, a γH2A binding mutant, *rtt107^{TK}* (T842A/K887M) (Li et al., 2012), greatly reduced the levels of chromatin-bound Nse6, Mms22, and Slx4 (Figures 6C-6E). Moreover, the effects of *RIM* mutants were epistatic with *rtt107^{TK}* (Figures 6C-6E). These results suggest that Rtt107 serves as a molecular bridge to connect multiple tetra-BRCT-binding proteins with chromatin.

Rtt107-mediated chromatin targeting of client proteins aids genome stability and replication

We hypothesized that the bridging function of Rtt107 relying on both its di- and tetra-BRCT domains is important for genome maintenance. This model predicts that *rtt107^{TK}* and *h2a^{S129A}* (Szilard et al., 2010), which abrogate Rtt107 di-BRCT–γH2A interaction while retaining its tetra-BRCT–RIM interactions, should exhibit similar or stronger defects compared to *RIM* mutants. Indeed, GCR and rDNA marker loss assays and chromosomal replication data supported this prediction (Figures 5B, 6B, and 6A). These findings strengthen our model and suggest that Rtt107 utilizes its two sets of BRCT domains to direct client proteins on chromatin and this critical for DNA replication and genome stability.

DISCUSSION

BRCT domain-mediated protein interactions are integral to the genome maintenance network. Our structural, biochemical, and mutagenesis data demonstrate that the compact Rtt107 tetra-BRCT structure recognizes a variety of unmodified peptides via a common bipartite binding strategy. Our *in vivo* findings identified new house-keeping roles of multiple Rtt107 interactions in genome maintenance and a concerted action of two types of BRCT domains in Rtt107 in targeting client proteins to chromatin during growth. Based on these insights into Rtt107 tetra-BRCT structure, its client-recognition mechanisms, and its collaboration with di-BRCT in controlling client proteins and genome maintenance, we propose a mechanistic model of how the Rtt107 master regulator regulates multiple genome functions by serving as a molecular bridge (Figure 6F and details below).

A higher-order tetra-BRCT structure and its client recognition mechanism

Our study shows that the Rtt107 tetra-BRCT structure is not simply a combined pair of di-BRCTs. The ability of multiple BRCT repeats to fold into a tetrahedral assembly rather than

a linear or planar form suggests that additional 'BRCT origami' may be possible. This finding underlines the importance of examining the entire region containing multiple BRCT domains rather than subsets of its repeats. Our data also show that the unique tetra-BRCT structure enables a different ligand recognition mechanism than that of di-BRCTs (more below). This first example (to our knowledge) of domain repeats forming a highly compact assembly to acquire new functions may be applicable to other repetitive domains generated by gene duplication during evolution.

Unlike classical di-BRCT domains that recognize phospho-Ser/Thr peptides, we showed that Rtt107 tetra-BRCT bound to multiple unphosphorylated ligands. This finding expands our perception of BRCT domain functions. Our data further demonstrate that Rtt107 tetra-BRCT uses a bipartite mechanism in client recognition, wherein RBIP recognizes the D/E-S/T-Q/E/T/N motif of the RIMs and a hydrophobic groove engages a hydrophobic region of RIMs (Figure 6G). We also found variations under this scheme. For example, while the electrostatic interface is more critical for Rtt107 interactions with Nse6 and Slx4, the Rtt107–Mms22 interaction also heavily relies on their hydrophobic interface. We found that $Rtt107_{NTD}$ interactions with additional RIMs from Scm3, Rad55 and Cdc7 were similar to those with Nse6 and Slx4. It is thus likely that Rtt107 tetra-BRCT recognizes the D/E-S/T-N/Q/E/T motif and relies on the hydrophobic interface to fine tune affinity in order to accommodate large numbers of ligands.

We suggest that the shared interaction mechanism of multiple Rtt107 client proteins ensures a binary interaction between Rtt107 and proteins of different activities, thus preventing promiscuity among different functions. As the two Slx4 RIMs use a similar mechanism to bind Rtt107 and show competition in Rtt107 association, they likely contribute to different Slx4–Rtt107 complexes. The specific mode by which Slx4 engages with Rtt107 may determine how they associate with additional proteins that have been previously identified (Gritenaite et al., 2014; Ohouo et al., 2010; Princz et al., 2017). Rtt107 could also use additional surfaces and protein modifications for regulating binding and increasing the plasticity of its interactomes. Indeed, Rtt107 has been shown to be phosphorylated and the RIM sequences contain concensus sites for CDK, DDK and Mec1 kinases (Rouse, 2004). As such, the Rtt107 interactom may be subject to protein modification-based regulation. Further exploration of these topics will further expand our understanding of the scope of the Rtt107 interactome and its regulation in the future.

Unique and concerted genomic effects of the Rtt107 interactions with client proteins

Our analyses of *RIM* alleles that specifically disrupt the Rtt107 interactions with Nse6, Mms22, or Slx4 reveal that these interactions constitutively support genome stability during growth, altering the view that BRCT domains mainly contribute to the DNA damage response. We found that Rtt107 interactions with Nse6, Mms22, or Slx4 all contribute to the maintenance of rDNA, a site highly prone to DNA fragility and instability. As rDNA also influences genomic stability and RNA and protein synthesis by organizing nucleoli, the Rtt107 interactome can link DNA stability to overall cellular fitness.

Although different Rtt107 interactions contribute to the same goal, each interaction also plays unique roles, as defects of different *RIM* mutants were buffered by distinct genes and

showed different levels of genome instability. These unique roles are linked to specific genome maintenance pathways mediated by Sgs1, Rrm3, and Esc2, and can extend beyond previously suggested functions under damage conditions, such as DNA damage checkpoint regulation or large replicon synthesis (Ohouo et al., 2013) (Hang et al., 2015). As Rtt107 client proteins affect a large spectrum of genome maintenance functions, including DNA replication, repair, and segregation, Rtt107-based network has a broad influence on genome fitness. The *RIM* mutants will provide tools for further mechanistic studies of the Rtt107-based network and accelerate the illumination of its entire spectrum of functions.

Collaboration of Rtt107 tetra- and di-BRCT domains in chromatin targeting of client proteins

We found that the Rtt107 tetra-BRCT domain acts in concert with its di-BRCT domain to target client proteins to chromatin, supporting a model wherein Rtt107 controls multiple client proteins function by targeting them to γH2A-containing chromatin during growth. Our findings unify and extend previous proposals made under genotoxic conditions for damage site localization (Balint et al., 2015; Leung et al., 2011). Importantly the current work provides a structural and mechanistic basis for these effects and demonstrates that a recruitment function safe-guards the genome during cycles of mitotic growth. Our findings also underline the importance of studying the integrated functions of different sets of BRCT domains within the same protein.

As γH2A can spread over several kilobases during growth (Strom et al., 2007; Szilard et al., 2010), Rtt107 likely affects vast tracts of the genome. Additionally, its tetra-BRCT interactors possess diverse activities, ranging from regulating different forms of protein modifications to direct DNA transactions, allowing Rtt107 to orchestrate diverse functions. As such, Rtt107 complements the other "hub" proteins to generate a repertoire of mechanisms that deliver different sets of factors to specific DNA and chromatin regions (Figure S7A). Together, they may provide a nuclear protein "zip-code system" that sorts proteins containing specific recognition peptides to different regions of DNA and chromatin. This system can provide a fine-tuning mechanism to complement the general protein sorting system.

As seen for Rtt107, the BRCT1-4 domains of the mammalian PTIP and fission yeast Brc1 also lack phospho-peptide binding sites, while their BRCT5-6 domains bind to γH2A (Li et al., 2012; Manke et al., 2003; Williams et al., 2010; Yan et al., 2011; Yu et al., 2003). We thus speculate that PTIP and Brc1 may act in a similar fashion to Rtt107, using their BRCT1-4 domains to recoganize unphosphorylated client proteins and target them to DNA replication and damage sites. While the tetra-BRCT fold is difficult to predict at the sequence level, RIM-like sequences are found in Nse6, Mms22, and Slx4 homologs from specieces closely related to budding yeast and in fission yeast, which has a large evolutionary distance from budding yeast, suggesting the conserveation of this sequence (Figures S7B-S7C). Thus, our findings can stimulate understanding of how multi-BRCT proteins recognize specific client proteins and control complex genome metabolism processes in other organisms.

STAR★METHODS

CONTACT FOR REAGENT AND RESOURCE SHARING

Further information and requests for resources and reagents should be directed to and will be fulfilled by, the Lead Contact, Xiaolan Zhao (zhaox1@mskcc.org).

EXPERIMENTAL MODEL AND SUBJECT DETAILS

Yeast strains are listed in the Key Resources Table.

METHOD DETAILS

Protein expression and purification.—Codon-optimized $Rtt107_{NTD}$ (residues 2-513) was fused to a GST tag and expressed from the pGEX-6P-1 vector in the BL21 (DE3) *Escherichia coli* strain. Cells grown at 37°C in 12 L TB (terrific broth) media were induced for protein expression with 0.2 mM IPTG for 16 h at 20°C. Cell pellets were resuspended in lysis buffer (50 mM Tris-HCl, pH 8.0, 400 mM NaCl, 10% glycerol, 1 mM PMSF, 1 μg/ml leupeptin, 1 μg/ml pepstatin, 5 mM benzamidine, and 4 mM β-mercaptoethanol) and sonicated. After ultracentrifugation to remove cell debris, supernatant was incubated with glutathione sepharose 4B beads for 2 h at 4°C. Beads were washed with lysis buffer and the $Rtt107_{NTD}$ protein was eluted with the addition of 15 mM reduced glutathione (Sigma). Following the removal of the GST tag by the PreScission protease, ion exchange (Mono Q column) and gel-filtration chromatography (Superdex 200 column) were used to purify untagged $Rtt107_{NTD}$ to close to homogeneity. Peak fractions containing $Rtt107_{NTD}$ were concentrated and stored at −80°C.

The GST tag was fused to $Nse6_{RIM}$ (residues 2-46), $Slx4_{RIM1}$ (residues 407-445), $Slx4_{RIM2}$ (residues 535-587), $Scm3_{RIM}$ (residues 165-223), $Rad55_{RIM}$ (residues 371-406), and $Cdc7_{RIM}$ (residues 470-507) peptides and the fusions proteins were expressed from the pGEX-6P-1 vector in the BL21 (DE3) strain. Cells grown at 37°C in 2 L LB media were induced for protein expression with 0.1 mM IPTG for 12 h at 24°C. The expressed proteins were first purified by binding to glutathione Sepharose 4B beads. For GST, $Slx4_{RIM1}$-GST, and $Slx4_{RIM2}$-GST, the proteins were further purified by gel-filtration chromatography (HiLoad 16/600 Superdex 200). For the other fusion proteins, GST tag was cleaved by the PreScission protease and the peptides were further purified by gel-filtration chromatography (HiLoad 16/600 Superdex 75).

6xHis-SUMO tagged $Mms22_{RIM}$ (residues 2-38) and $Slx4_{RIM1}$ (residues 407-445) peptides were expressed from the pET-28a vector and purified as described above, except that Ni-NTA agarose beads (QIAGEN) were used for affinity purification and 10 mM imidazole was included in the lysis buffer. The tag was removed by the Ulp1 protease and the $Mms22_{RIM}$ or the $Slx4_{RIM1}$ peptide was further purified by gel-filtration chromatography (HiLoad 16/600 Superdex 75). Glutathione beads, chromatography columns, and proteases used in this study were purchased from GE Healthcare.

Crystallization, data collection, and structure determination.—Crystals of purified $Rtt107_{NTD}$ were grown by sitting-drop vapor diffusion. The precipitant well

solution consisted of 1.8 M $(NH_4)_2SO_4$, 50 mM pH 5.8 sodium cacodylate, 5 mM $Mg(OAc)_2$, and 0.5 mM spermine. Crystals were gradually transferred into a harvesting solution containing 2 M $(NH_4)_2SO_4$, 50 mM pH 5.8 sodium cacodylate, 15 mM $Mg(OAc)_2$, 1 mM spermine, and 25% glycerol, followed by flash-freezing in liquid nitrogen for storage. For preparation of a mercury derivative, ethyl mercuric phosphate was soaked into the $Rtt107_{NTD}$ crystals for 1 h at 4°C.

The $Rtt107_{NTD}$ protein was mixed with each ligand peptide at a molar ratio 1:2 to form the corresponding complex. The $Rtt107_{NTD}$–$Nse6_{RIM}$ complex crystals were grown by sitting-drop vapor diffusion with a well solution containing 22% PEG 3350, 0.1 M pH 6.0 Bis-Tris, and 0.2 M NH4OAc. For the $Rtt107_{NTD}$–$Slx4_{RIM2}$ complex, the well solution contained 10% PEG 6000, 0.1 M pH 7.0 HEPES, and silver bullets additive G9 (Hampton Research). For the $Rtt107_{NTD}$–$Mms22_{RIM}$ complex, the well solution contained 25% PEG 3350, 0.1 pH 6.0 M Bis-Tris, and 0.2 M $MgCl_2$. All crystals were gradually transferred into harvesting solution and flash-frozen in liquid nitrogen for storage.

Datasets were collected under cryogenic conditions (100K) at Advanced Photon Source (APS) beamline 21ID-D and 24ID-C. A 2.8 Å Hg-SAD (single-wavelength anomalous dispersion) dataset of $Rtt107_{NTD}$ was collected at the wavelength of 0.97623 Å and was processed by HKL3000 (Minor et al., 2006). Three mercury atoms were located and refined, and the single-wavelength anomalous diffraction data phases were calculated using Phenix (Adams et al., 2010). The initial SAD map was substantially improved by solvent flattening. An initial model was automatically built into the modified experiment electron density. The model was then refined with a native data set with a 2.3 Å resolution with manual building in Coot (Emsley et al., 2010). The $Rtt107_{NTD}$–$Nse6_{RIM}$, $Rtt107_{NTD}$–$Slx4_{RIM2}$ and $Rtt107_{NTD}$–$Mms22_{RIM}$ complex structures were solved by molecular replacement with the $Rtt107_{NTD}$ native structure as the searching model. The models were refined using Phenix, together with manual building in Coot. All the structural figures were generated using PyMOL (www.pymol.org).

Isothermal titration calorimetry.—Dissociation constants of the $Rtt107_{NTD}$ interactions with ligand peptides were determined using an iTC200 calorimeter (MicroCal). Binding enthalpies were monitored when peptides were injected into cells containing $Rtt107_{NTD}$ in 25 mM pH 8.0 Tris-HCl and 150 mM NaCl at 16°C. As controls, peptides were injected into buffer lacking $Rtt107_{NTD}$. Three independent experiments were performed for each interaction, and data were calculated and fitted using Origin 7 software (OriginLab).

Yeast strain construction and genetic manipulation.—Yeast strains are derivatives of W1588-4C, a *RAD5* variety of W303 (*MATa ade2-1 can1-100 ura3-1 his3-11,15 leu2-3,112 trp1-1 rad5-535*) (Zhao et al., 1998). Strains are listed in Table S1. All proteins were expressed from their endogenous loci. Protein tagging, gene deletion, and point mutation were generated following standard PCR-based or CRISPR-Cas9 methods (DiCarlo et al., 2013). A GCR assay strain in the W303 background was constructed following a previously described procedure (Putnam et al., 2009). Briefly, the endogenous *URA3* ORF (Chr 5: 116167-116970) and *CAN1* ORF (Chr 5: 31694-33466) were deleted by CRISPR-Cas9 method to prevent assay interference. To insert the *URA3-CAN1* cassette at the

YEL068C locus (Chr 5: 25646-25978), the pRDK1379 plasmid (KEY RESOURCES TABLE) was digested with PvuII (NEB) and transformed into yeast cells. We verified that GCR rates for wild-type and sgs1 strains were similar to those reported previously (Putnam et al., 2009).

All genetically altered loci were verified by sequencing. Standard yeast genetic manipulation was used for tetrad analyses and spotting assays. Pictures were taken after plates were incubated for 2 days at 30°C. To determine doubling time, OD_{600} of yeast cultures grown in YPD media were assessed every 10 min using SpectraMax M5 microplate spectrophotometer. OD_{600} values from early-mid log phase were used to calculate doubling time (T_D) using the formula: $T_D = \ln(2/k)$. k (constant of growth) = $(\ln(N_X) - \ln(N_0))/(T_X - T_0)$; N_0 and N_X represent OD_{600} values at time points T_0 and T_X (in minutes), respectively.

Yeast two-hybrid assay.—The yeast two-hybrid assays were performed as previously described (Wan et al., 2015). Briefly, $Rtt107_{NTD}$, as well as various fragments of Nse6, Slx4, Mms22, Scm3, Rad55, and Cdc7 was cloned into pBTM116 (BD) and pACT2 (AD) vectors (Clontech) at the BamHI and XhoI sites (KEY RESOURCES TABLE). Mutations were made by site-directed mutagenesis using the QuikChange mutagenesis kit (Stratagene). Yeast cells harboring BD and AD plasmids were selected on SC-Leu-Trp plates. β-galactosidase activities were measured according to Clontech Matchmaker yeast two-hybrid protocol with o-nitrophenyl β-D-galactopyranoside (ONPG) as substrate. The averages from three transformants were calculated and error bars represent standard deviations.

Co-immunoprecipitation.—Log-phase cells were harvested and resuspended in IP buffer (20 mM pH 8.0 HEPES-KOH, 150 mM KOAc, 2 mM $Mg(OAc)_2$, 10% glycerol, 5 μM leupeptin, 1mM PMSF, 1 mM NaF, 0.5 mM Na_3VO_4, 2 mM β-glycerophosphate, Sigma protease inhibitor cocktail, 0.6% Triton X-100), followed by lysis with glass beads in a FastPrep-24 homogenizer (MP Biomedicals). Benzonase (EMD Millipore) was added to degrade DNA. Supernatant after centrifugation was incubated with IgG-sepharose (binds TAP), anti-FLAG, or anti-HA beads (Sigma) for 2 h at 4°C. After washing beads with IP buffer, proteins were eluted with loading buffer (125 mM pH 6.8 Tris-HCl, 4% SDS, 20% glycerol, 0.02% bromophenol blue) at 85°C for 5 min. DTT was added to protein samples before assaying by SDS-PAGE on 4–20% gels (Bio-Rad). Antibodies used in Western blotting include anti-HA (Santa Cruz Biotech), anti-Myc (Bio X Cell), anti-Flag (Sigma), anti-TAP (Sigma).

PFGE analysis.—G1-arrested cells were released to S phase for 45 min and embedded into agarose plugs for PFGE analyses as previously described (Cremona et al., 2012). Briefly, plugs were treated with zymolyase (20T, MP Biomedicals), proteinase K, and lauroylsarcosine to permeabilize cells. Chromosomes were separated by 1% agarose (Bio-Rad) gels in 0.5× TBE buffer using the Bio-Rad CHEF-DR III PFGE system. Gel running conditions were 70–160 s switch time, 5.5 V/cm voltage gradient, and 106° angle for 15 h at 12°C. After electrophoresis, chromosomes were transferred to Hybond-XL nylon membranes (GE) for Southern blotting using an [α-^{32}P]-dCTP-labeled rDNA probe. Autoradiographic signals were scanned by Typhoon FLA 9500 phosphoimager (GE), and rDNA replication efficiency was assessed by calculating the ratio of chromosome band

signals to the corresponding well signals after adjusting for background signals. Quantification of chromosomal bands was performed using the ImageJ software.

GCR rate measurement.—We determined GCR rates in W303 strain background according to fluctuation analysis described previously (Putnam and Kolodner, 2010). For each genotype, at least 9 cultures were examined in at least two different strains. Yeast cells were washed and serial dilutions were plated on SC+5-FOA+Can (FC) and SC plates. Cells which lose the *CAN1-URA3* cassette are resistant to canavanine and 5-FOA. After inoculation of plates for 3-4 days at 30°C, colonies on FC and SC plates were counted. GCR rates (R_G) were calculated by the following equation: $R_G = m/N_T$, wherein m (1.24 + ln[m]) − N_{FC} = 0. m: mutational events, N_{FC}: number of colonies on FC plates, N_T: number of total cells spread on the FC plates, which was deduced from the number of colonies on SC plates. The upper and lower 95% confidence intervals (95% CI) were calculated as described (Putnam and Kolodner, 2010).

rDNA marker loss frequency.—The loss of the *ADE2-CAN1* cassette inside the rDNA array was examined as previously described (Fritze et al., 1997). Briefly, cells were grown for equal doublings to stationary phase. Cells were plated on SC media for total cell counts. Cells were also plated on canavanine-containing media (SC+Can), then replica plated to media lacking adenine (SC-Ade). Marker loss frequency (F_R) was calculated as described previously (Bernstein et al., 2011). using the following formula: $F_R = (N_{Can}-N_{Ade})/N_C$, wherein N_{Can} = number of colonies on SC+Can plates, N_{Ade} = number of colonies on SC-Ade plates, and N_C = number of cells plated on SC+Can plates. Marker loss frequencies of mutant strains were normalized to wide-type.

Chromatin fractionation.—Chromatin fractionation was performed as described previously (Chung and Zhao, 2015). In brief, spheroplasts from log-phase cells were lysed using extraction buffer (20 mM pH 6.6 PIPES-KOH, 150 mM KOAc, 2 mM Mg(OAc)$_2$, 1 mM NaF, 0.5 mM Na$_3$VO$_4$, 1 × Sigma protease inhibitors, 1% Triton X-100) for 5 min on ice. After centrifugation at 16,000 g for 15 min on a sucrose cushion, chromatin pellets were washed and resuspended with extraction buffer. Protein loading buffer was added to cell extract and chromatin fraction and boiled for 5 min before SDS-PAGE followed by Western blotting. Pgk1 and histone H3 are markers for non-chromatin and chromatin associated proteins, respectively. Antibodies used are as described above, except that anti-Pgk1 (Invitrogen) and anti-H3 (Abcam) were also used.

***In vitro* competition assay.—**100 μg Slx4$_{RIM2}$-GST or GST protein and 60 μg Rtt107$_{NTD}$ were incubated in 50 μl binding buffer (25 mM pH 8.0 Tris-HCl, 150 mM NaCl and 1 mM DTT) for 15 min at 4°C. Mms22$_{RIM}$, Slx4$_{RIM1}$ or Nse6$_{RIM}$ used added into the complex in a ratio (Rtt107$_{NTD}$: Slx4$_{RIM2}$-GST: competitor = 1: 2: 4 in Figure 4G) to compete for 15 min. The mixture was incubated with 10 μl of glutathione agarose resin to retain Slx4$_{RIM2}$-GST or GST for 1 h. After washing the resin five times with 100 μl of binding buffer, bound proteins were eluted with 20 μl SDS protein sample buffer. 2 μl eluted samples and input samples (5% protein of competition assay) were analyzed by 4%–20% gradient SDS-PAGE and Coomassie blue staining. Similar procedure was used for Figure

4H, except that peptides and their concentrations varied as indicated in the graph. Quantification of protein bands was performed using the ImageJ software.

QUANTIFICATION AND STATISTICAL ANALYSIS

Quantification of PFGE data (Figure 6A) and protein bands on gels (Figures S5B and S5C) was performed using the ImageJ software. Statistical analyses were performed using the GraphPad Prism 7 software, except that the ITC data were analyzed using the Origin 7 software. Additional details of statistical analyses are described in Figure Legends and in Results. Data are represented as mean ± standard deviation, except that for the GCR assay data, error bars are the 95% confidence intervals.

DATA AND SOFTWARE AVAILABILITY

The following coordinates have been deposited in the RCSB Protein Data Bank: apo-Rtt107$_{NTD}$ (6J0V); Rtt107$_{NTD}$–Nse6$_{RIM}$ complex (6J0W); Rtt107$_{NTD}$–Mms22$_{RIM}$ complex (6J0X); Rtt107$_{NTD}$– Slx4$_{RIM2}$ complex (6J0Y).

Supplementary Material

Refer to Web version on PubMed Central for supplementary material.

REFERENCES

Adams PD, Afonine PV, Bunkoczi G, Chen VB, Davis IW, Echols N, Headd JJ, Hung LW, Kapral GJ, Grosse-Kunstleve RW, et al. (2010). PHENIX: a comprehensive Python-based system for macromolecular structure solution. Acta Crystallogr D Biol Crystallogr 66, 213–221. [PubMed: 20124702]

Aragon L (2018). The Smc5/6 Complex: New and Old Functions of the Enigmatic Long-Distance Relative. Annu Rev Genet 52, 89–107. [PubMed: 30476445]

Balint A, Kim T, Gallo D, Cussiol JR, Bastos de Oliveira FM, Yimit A, Ou J, Nakato R, Gurevich A, Shirahige K, et al. (2015). Assembly of Slx4 signaling complexes behind DNA replication forks. EMBO J 34, 2182–2197. [PubMed: 26113155]

Bernstein KA, Reid RJ, Sunjevaric I, Demuth K, Burgess RC, and Rothstein R (2011). The Shu complex, which contains Rad51 paralogues, promotes DNA repair through inhibition of the Srs2 anti-recombinase. Mol Biol Cell 22, 1599–1607. [PubMed: 21372173]

Chin JK, Bashkirov VI, Heyer WD, and Romesberg FE (2006). Esc4/Rtt107 and the control of recombination during replication. DNA Repair (Amst) 5, 618–628. [PubMed: 16569515]

Chung I, and Zhao X (2015). DNA break-induced sumoylation is enabled by collaboration between a SUMO ligase and the ssDNA-binding complex RPA. Genes Dev 29, 1593–1598. [PubMed: 26253534]

Clapperton JA, Manke IA, Lowery DM, Ho T, Haire LF, Yaffe MB, and Smerdon SJ (2004). Structure and mechanism of BRCA1 BRCT domain recognition of phosphorylated BACH1 with implications for cancer. Nat Struct Mol Biol 11, 512–518. [PubMed: 15133502]

Costanzo M, VanderSluis B, Koch EN, Baryshnikova A, Pons C, Tan G, Wang W, Usaj M, Hanchard J, Lee SD, et al. (2016). A global genetic interaction network maps a wiring diagram of cellular function. Science 353.

Cremona CA, Sarangi P, Yang Y, Hang LE, Rahman S, and Zhao X (2012). Extensive DNA damage-induced sumoylation contributes to replication and repair and acts in addition to the mec1 checkpoint. Mol Cell 45, 422–432. [PubMed: 22285753]

Cussiol JR, Dibitetto D, Pellicioli A, and Smolka MB (2017). Slx4 scaffolding in homologous recombination and checkpoint control: lessons from yeast. Chromosoma 126, 45–58. [PubMed: 27165041]

DiCarlo JE, Norville JE, Mali P, Rios X, Aach J, and Church GM (2013). Genome engineering in Saccharomyces cerevisiae using CRISPR-Cas systems. Nucleic Acids Res 41, 4336–4343. [PubMed: 23460208]

Duro E, Lundin C, Ask K, Sanchez-Pulido L, MacArtney TJ, Toth R, Ponting CP, Groth A, Helleday T, and Rouse J (2010). Identification of the MMS22L-TONSL complex that promotes homologous recombination. Mol Cell 40, 632–644. [PubMed: 21055984]

Duro E, Vaisica JA, Brown GW, and Rouse J (2008). Budding yeast Mms22 and Mms1 regulate homologous recombination induced by replisome blockage. DNA Repair (Amst) 7, 811–818. [PubMed: 18321796]

Emsley P, Lohkamp B, Scott WG, and Cowtan K (2010). Features and development of Coot. Acta Crystallogr D Biol Crystallogr 66, 486–501. [PubMed: 20383002]

Fritze CE, Verschueren K, Strich R, and Easton Esposito R (1997). Direct evidence for SIR2 modulation of chromatin structure in yeast rDNA. EMBO J 16, 6495–6509. [PubMed: 9351831]

Gritenaite D, Princz LN, Szakal B, Bantele SC, Wendeler L, Schilbach S, Habermann H, Matos J, Lisby M, Branzei D, et al. (2014). A cell cycle-regulated Slx4-Dpb11 complex promotes the resolution of DNA repair intermediates linked to stalled replication. Genes Dev 28, 1604–1619. [PubMed: 25030699]

Hang LE, Peng J, Tan W, Szakal B, Menolfi D, Sheng Z, Lobachev K, Branzei D, Feng W, and Zhao X (2015). Rtt107 Is a Multi-functional Scaffold Supporting Replication Progression with Partner SUMO and Ubiquitin Ligases. Mol Cell 60, 268–279. [PubMed: 26439300]

Jowsey PA, Doherty AJ, and Rouse J (2004). Human PTIP facilitates ATM-mediated activation of p53 and promotes cellular resistance to ionizing radiation. J Biol Chem 279, 55562–55569. [PubMed: 15456759]

Kim Y, Lach FP, Desetty R, Hanenberg H, Auerbach AD, and Smogorzewska A (2011). Mutations of the SLX4 gene in Fanconi anemia. Nat Genet 43, 142–146. [PubMed: 21240275]

Koonin EV, Altschul SF, and Bork P (1996). BRCA1 protein products … Functional motifs… Nat Genet 13, 266–268. [PubMed: 8673121]

Kuzmin E, VanderSluis B, Wang W, Tan G, Deshpande R, Chen Y, Usaj M, Balint A, Mattiazzi Usaj M, van Leeuwen J, et al. (2018). Systematic analysis of complex genetic interactions. Science 360.

Leung GP, Lee L, Schmidt TI, Shirahige K, and Kobor MS (2011). Rtt107 is required for recruitment of the SMC5/6 complex to DNA double strand breaks. J Biol Chem 286, 26250–26257. [PubMed: 21642432]

Li X, Liu K, Li F, Wang J, Huang H, Wu J, and Shi Y (2012). Structure of C-terminal tandem BRCT repeats of Rtt107 protein reveals critical role in interaction with phosphorylated histone H2A during DNA damage repair. J Biol Chem 287, 9137–9146. [PubMed: 22262834]

Luciano P, Dehe PM, Audebert S, Geli V, and Corda Y (2015). Replisome function during replicative stress is modulated by histone h3 lysine 56 acetylation through Ctf4. Genetics 199, 1047–1063. [PubMed: 25697176]

Manke IA, Lowery DM, Nguyen A, and Yaffe MB (2003). BRCT repeats as phosphopeptide-binding modules involved in protein targeting. Science 302, 636–639. [PubMed: 14576432]

Menolfi D, Delamarre A, Lengronne A, Pasero P, and Branzei D (2015). Essential Roles of the Smc5/6 Complex in Replication through Natural Pausing Sites and Endogenous DNA Damage Tolerance. Mol Cell 60, 835–846. [PubMed: 26698660]

Minor W, Cymborowski M, Otwinowski Z, and Chruszcz M (2006). HKL-3000: the integration of data reduction and structure solution--from diffraction images to an initial model in minutes. Acta Crystallogr D Biol Crystallogr 62, 859–866. [PubMed: 16855301]

Mullen JR, Kaliraman V, Ibrahim SS, and Brill SJ (2001). Requirement for three novel protein complexes in the absence of the Sgs1 DNA helicase in Saccharomyces cerevisiae. Genetics 157, 103–118. [PubMed: 11139495]

O'Donnell L, Panier S, Wildenhain J, Tkach JM, Al-Hakim A, Landry MC, Escribano-Diaz C, Szilard RK, Young JT, Munro M, et al. (2010). The MMS22L-TONSL complex mediates recovery from replication stress and homologous recombination. Mol Cell 40, 619–631. [PubMed: 21055983]

Ohouo PY, Bastos de Oliveira FM, Almeida BS, and Smolka MB (2010). DNA damage signaling recruits the Rtt107-Slx4 scaffolds via Dpb11 to mediate replication stress response. Mol Cell 39, 300–306. [PubMed: 20670896]

Ohouo PY, Bastos de Oliveira FM, Liu Y, Ma CJ, and Smolka MB (2013). DNA-repair scaffolds dampen checkpoint signalling by counteracting the adaptor Rad9. Nature 493, 120–124. [PubMed: 23160493]

Pan X, Ye P, Yuan DS, Wang X, Bader JS, and Boeke JD (2006). A DNA integrity network in the yeast Saccharomyces cerevisiae. Cell 124, 1069–1081. [PubMed: 16487579]

Princz LN, Wild P, Bittmann J, Aguado FJ, Blanco MG, Matos J, and Pfander B (2017). Dbf4-dependent kinase and the Rtt107 scaffold promote Mus81-Mms4 resolvase activation during mitosis. EMBO J 36, 664–678. [PubMed: 28096179]

Putnam CD, Hayes TK, and Kolodner RD (2009). Specific pathways prevent duplication-mediated genome rearrangements. Nature 460, 984–989. [PubMed: 19641493]

Putnam CD, and Kolodner RD (2010). Determination of gross chromosomal rearrangement rates. Cold Spring Harb Protoc 2010, pdb prot5492.

Roberts TM, Kobor MS, Bastin-Shanower SA, Ii M, Horte SA, Gin JW, Emili A, Rine J, Brill SJ, and Brown GW (2006). Slx4 regulates DNA damage checkpoint-dependent phosphorylation of the BRCT domain protein Rtt107/Esc4. Mol Biol Cell 17, 539–548. [PubMed: 16267268]

Rouse J (2004). Esc4p, a new target of Mec1p (ATR), promotes resumption of DNA synthesis after DNA damage. EMBO J 23, 1188–1197. [PubMed: 14988729]

Shakya R, Reid LJ, Reczek CR, Cole F, Egli D, Lin CS, deRooij DG, Hirsch S, Ravi K, Hicks JB, et al. (2011). BRCA1 tumor suppression depends on BRCT phosphoprotein binding, but not its E3 ligase activity. Science 334, 525–528. [PubMed: 22034435]

Sheedy DM, Dimitrova D, Rankin JK, Bass KL, Lee KM, Tapia-Alveal C, Harvey SH, Murray JM, and O'Connell MJ (2005). Brc1-mediated DNA repair and damage tolerance. Genetics 171, 457–468. [PubMed: 15972456]

Shiozaki E, Gu L, Yan N, and Shi Y (2004). Structure of the BRCT repeats of BRCA1 bound to a BACH1 phosphopeptide: implications for signaling. Mol Cell 14, 405–412. [PubMed: 15125843]

Sollier J, Driscoll R, Castellucci F, Foiani M, Jackson SP, and Branzei D (2009). The Saccharomyces cerevisiae Esc2 and Smc5-6 proteins promote sister chromatid junction-mediated intra-S repair. Mol Biol Cell 20, 1671–1682. [PubMed: 19158389]

Strom L, Karlsson C, Lindroos HB, Wedahl S, Katou Y, Shirahige K, and Sjogren C (2007). Postreplicative formation of cohesion is required for repair and induced by a single DNA break. Science 317, 242–245. [PubMed: 17626884]

Szilard RK, Jacques PE, Laramee L, Cheng B, Galicia S, Bataille AR, Yeung M, Mendez M, Bergeron M, Robert F, et al. (2010). Systematic identification of fragile sites via genome-wide location analysis of gamma-H2AX. Nat Struct Mol Biol 17, 299–305. [PubMed: 20139982]

Tong AH, Lesage G, Bader GD, Ding H, Xu H, Xin X, Young J, Berriz GF, Brost RL, Chang M, et al. (2004). Global mapping of the yeast genetic interaction network. Science 303, 808–813. [PubMed: 14764870]

Torres-Rosell J, Machin F, Farmer S, Jarmuz A, Eydmann T, Dalgaard JZ, and Aragon L (2005). SMC5 and SMC6 genes are required for the segregation of repetitive chromosome regions. Nat Cell Biol 7, 412–419. [PubMed: 15793567]

van der Crabben SN, Hennus MP, McGregor GA, Ritter DI, Nagamani SC, Wells OS, Harakalova M, Chinn IK, Alt A, Vondrova L, et al. (2016). Destabilized SMC5/6 complex leads to chromosome breakage syndrome with severe lung disease. J Clin Invest 126, 2881–2892. [PubMed: 27427983]

Wan B, Hang LE, and Zhao X (2016). Multi-BRCT scaffolds use distinct strategies to support genome maintenance. Cell Cycle 15, 2561–2570. [PubMed: 27580271]

Wan B, Tang T, Upton H, Shuai J, Zhou Y, Li S, Chen J, Brunzelle JS, Zeng Z, Collins K, et al. (2015). The Tetrahymena telomerase p75-p45-p19 subcomplex is a unique CST complex. Nat Struct Mol Biol 22, 1023–1026. [PubMed: 26551074]

Williams JS, Williams RS, Dovey CL, Guenther G, Tainer JA, and Russell P (2010). gammaH2A binds Brc1 to maintain genome integrity during S-phase. EMBO J 29, 1136–1148. [PubMed: 20094029]

Williams RS, Lee MS, Hau DD, and Glover JN (2004). Structural basis of phosphopeptide recognition by the BRCT domain of BRCA1. Nat Struct Mol Biol 11, 519–525. [PubMed: 15133503]

Woods NT, Mesquita RD, Sweet M, Carvalho MA, Li X, Liu Y, Nguyen H, Thomas E, Iversen ES Jr., Marsillac S, et al. (2012). Charting the landscape of tandem BRCT domain-mediated protein interactions. Sci Signal 5, rs6. [PubMed: 22990118]

Yan W, Shao Z, Li F, Niu L, Shi Y, Teng M, and Li X (2011). Structural basis of gammaH2AX recognition by human PTIP BRCT5-BRCT6 domains in the DNA damage response pathway. FEBS Lett 585, 3874–3879. [PubMed: 22064073]

Yu X, Chini CC, He M, Mer G, and Chen J (2003). The BRCT domain is a phospho-protein binding domain. Science 302, 639–642. [PubMed: 14576433]

Zappulla DC, Maharaj AS, Connelly JJ, Jockusch RA, and Sternglanz R (2006). Rtt107/Esc4 binds silent chromatin and DNA repair proteins using different BRCT motifs. BMC Mol Biol 7, 40. [PubMed: 17094803]

Zhao X, Muller EG, and Rothstein R (1998). A suppressor of two essential checkpoint genes identifies a novel protein that negatively affects dNTP pools. Mol Cell 2, 329–340. [PubMed: 9774971]

Highlights

- Four BRCT units from the Rtt107 protein form a compact higher-order assembly.

- Rtt107 tetra-BRCT recognizes multiple unmodified ligands via a consensus motif.

- Rtt107 binding to genome stability factors provides constitutive genome protection.

- Rtt107's tetra- and di-BRCT domains act in concert to recruit proteins to chromatin.
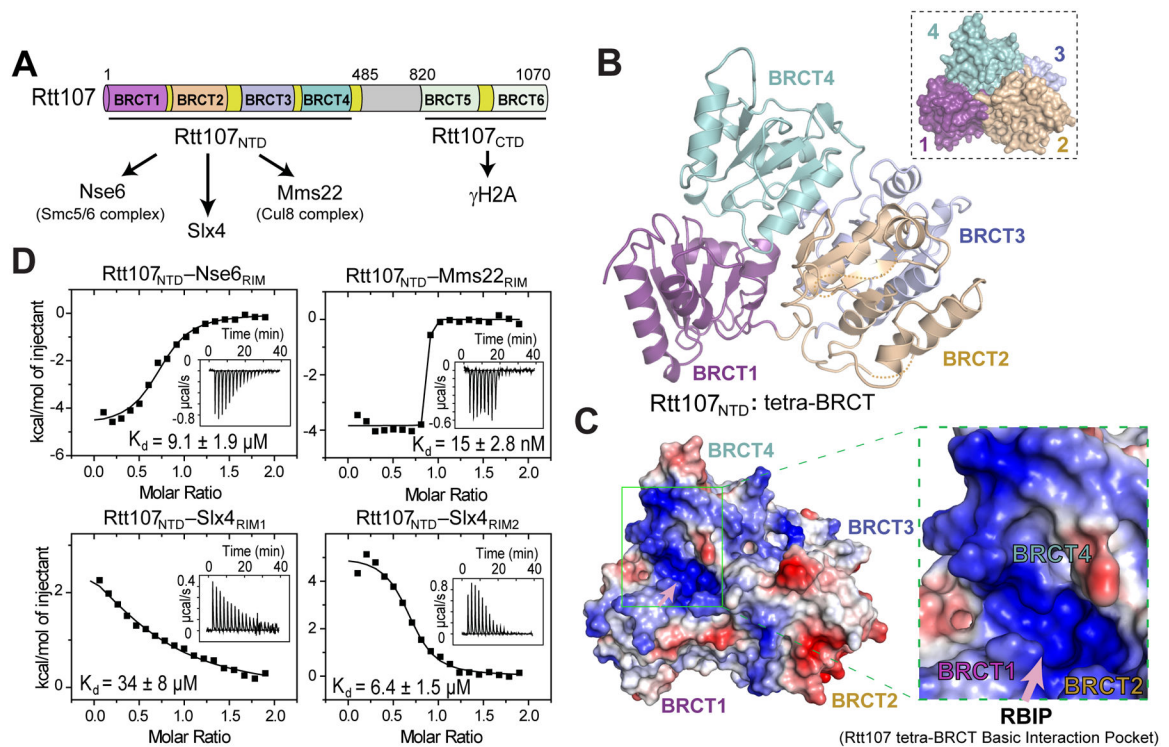
Figure 1. Rtt107$_{NTD}$ forms a compact tetrahedral structure and recognizes phospho-free peptide ligands.

(A) Schematic of Rtt107 domains and interacting proteins.

(B) Ribbon view of the Rtt107$_{NTD}$ structure. Inset shows the surface diagram of the four BRCT repeats, each in a different color.

(C) Electrostatic surface representation of Rtt107$_{NTD}$. RBIP is labeled with an arrow in an enlarged view on the right.

(D) ITC measurement of binding affinities of distinct RIM peptides toward Rtt107$_{NTD}$. See also Figure S1.
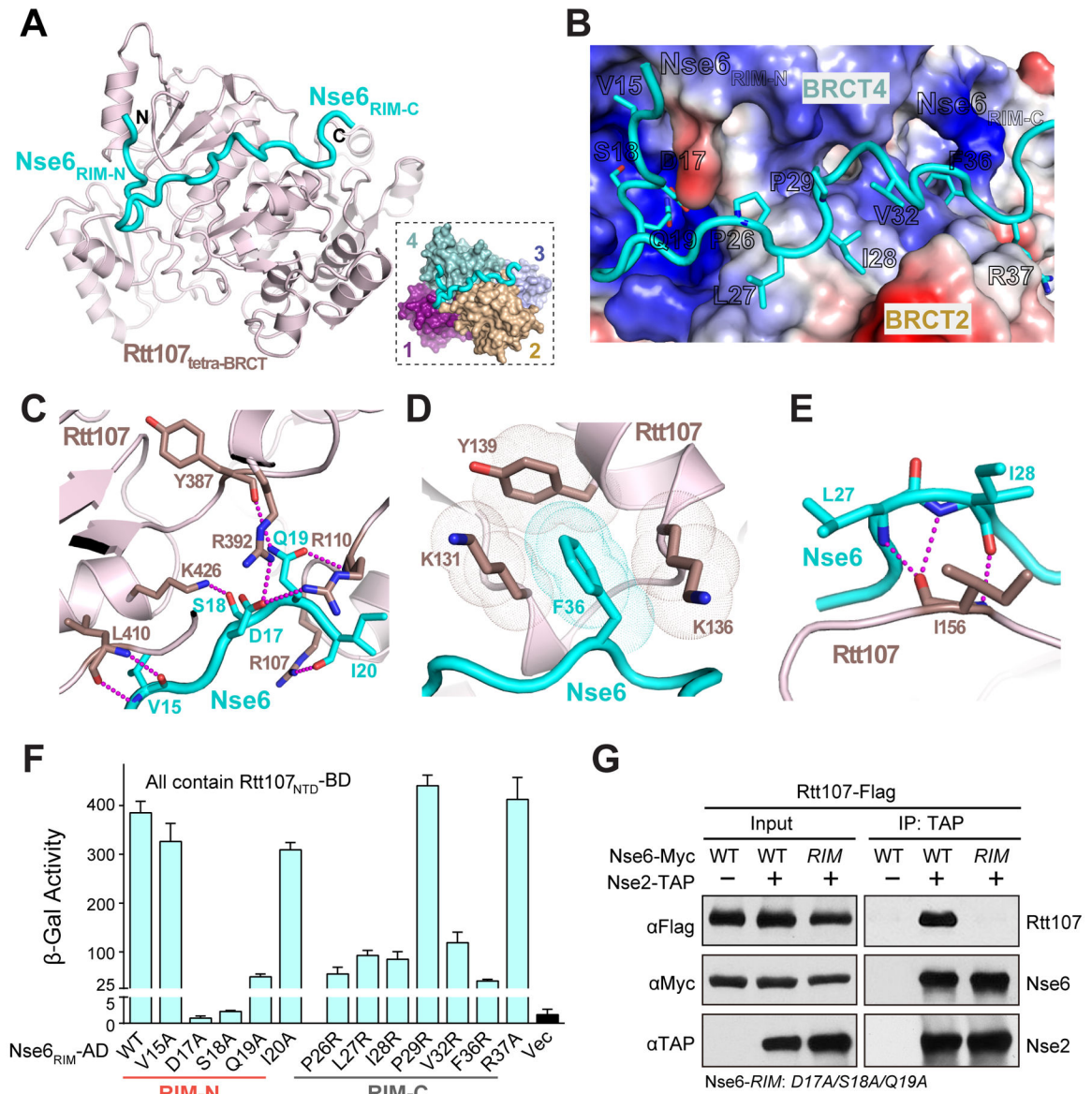
Figure 2. The structure of the Rtt107_NTD–Nse6_RIM complex reveals a bipartite interface.
(**A**) Overall structure of Rtt107_NTD (pink) bound to Nse6_RIM (cyan). A surface diagram is shown in the inset.

(**B**) The Nse6_RIM peptide forms two interfaces with the Rtt107 tetra-BRCT. Electrostatic surface of Rtt107_NTD and key Nse6_RIM contacts are shown.

(**C-E**) Close-up views of the Nse6_RIM and Rtt107_NTD interface. (**C**) The Nse6_RIM-N DSQ$_{17-19}$ motif forms multiple electrostatic interactions with Rtt107 BRCT1 and -4 residues. (**D**) The side chain of F36 in Nse6_RIM-C forms hydrophobic interactions with three Rtt107 residues. (**E**) Main chain hydrogen-bonding interactions between Nse6_RIM-C and Rtt107_NTD.

(**F**) The effects of mutating Nse6 residues on the Rtt107_NTD Y2H interaction.

(G) *nse6-RIM* abolishes the interaction with Rtt107, but not with Nse2. Immunoprecipitation of TAP-tagged Nse2 pulled down both wild-type Nse6 and Nse6[RIM] mutant proteins, but only pulled down Rtt107 if Nse6 was wildtype.
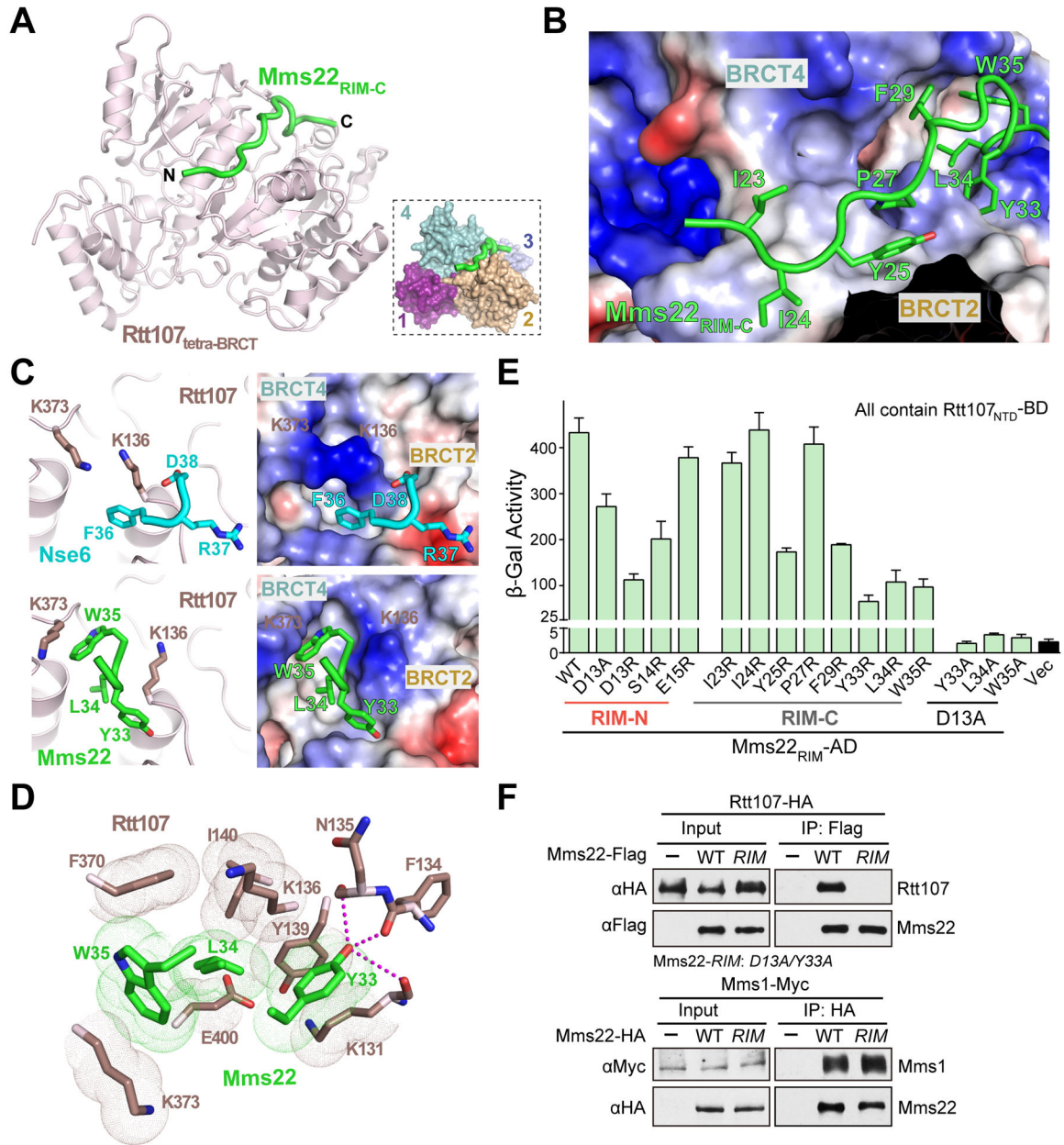
See also Figure S2, S3 and S4.

Figure 3. The Rtt107$_{NTD}$–Mms22$_{RIM}$ interaction entails a bipartite mode but has distinct features.

(**A**) Overall structure of the Rtt107$_{NTD}$ (pink) bound to Mms22$_{RIM}$ (green).

(**B**) Mms22$_{RIM-C}$ binds to a hydrophobic groove formed by Rtt107$_{NTD}$ BRCT2 and –4. Mms22$_{RIM-C}$ peptide (green, stick) and the Rtt107$_{NTD}$ groove (electrostatic surface) are shown.

(**C**) Comparison of hydrophobic interfaces between the Rtt107$_{NTD}$–Nse6$_{RIM}$ complex and the Rtt107$_{NTD}$–Mms22$_{RIM}$ complex. Rtt107$_{NTD}$ is shown as ribbon (left) and electrostatic surface representation (right).

(**D**) Close-up views of the interface between Rtt107$_{NTD}$ and Mms22$_{RIM-C}$. Hydrophobic interactions and hydrogen-bonds are indicated by dots and dashed lines, respectively.

(E) Summary of the effects of Mms22 mutations on the Rtt107$_{NTD}$ Y2H interaction.

(F) *mms22-RIM* abolishes the interaction with Rtt107 but not with Mms1 *in vivo*.
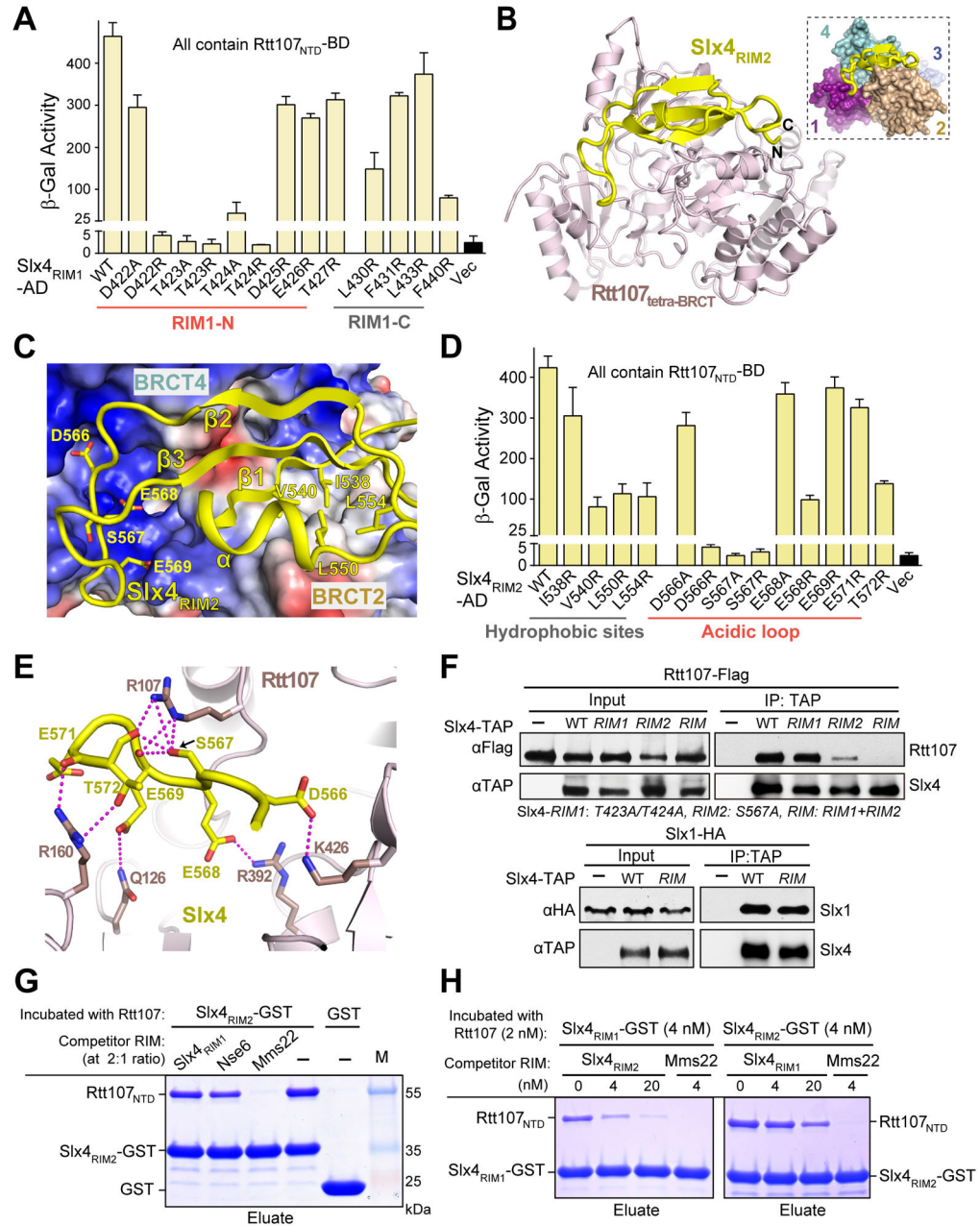
See also Figure S2, S3 and S4.

Figure 4. Shared and unique features of Rtt107 interactions with two Slx4 regions.

(A) Effects of Slx4$_{RIM1}$ mutations on the Rtt107$_{NTD}$ Y2H interaction.

(B) Overall structure of Rtt107$_{NTD}$ (pink) bound to Slx4$_{RIM2}$ (yellow).

(C) The interface between Slx4$_{RIM2}$ and Rtt107$_{NTD}$. Rtt107$_{NTD}$ is shown in electrostatic surface representation and Slx4$_{RIM2}$ in ribbon view.

(D) Effects of Slx4$_{RIM2}$ mutations on the Rtt107$_{NTD}$ Y2H interaction.

(E) Close-up view of the electrostatic interaction between Slx4$_{RIM2}$ and Rtt107$_{NTD}$.

(F) Mutating residues of the two Slx4 RIM regions affects the association with Rtt107 but not with Slx1 as examined by co-immunoprecipitation.

(G-H) *In vitro* competition assays among RIM peptides. Experimental procedures and input protein levels are included in Figures S5A-S5C.
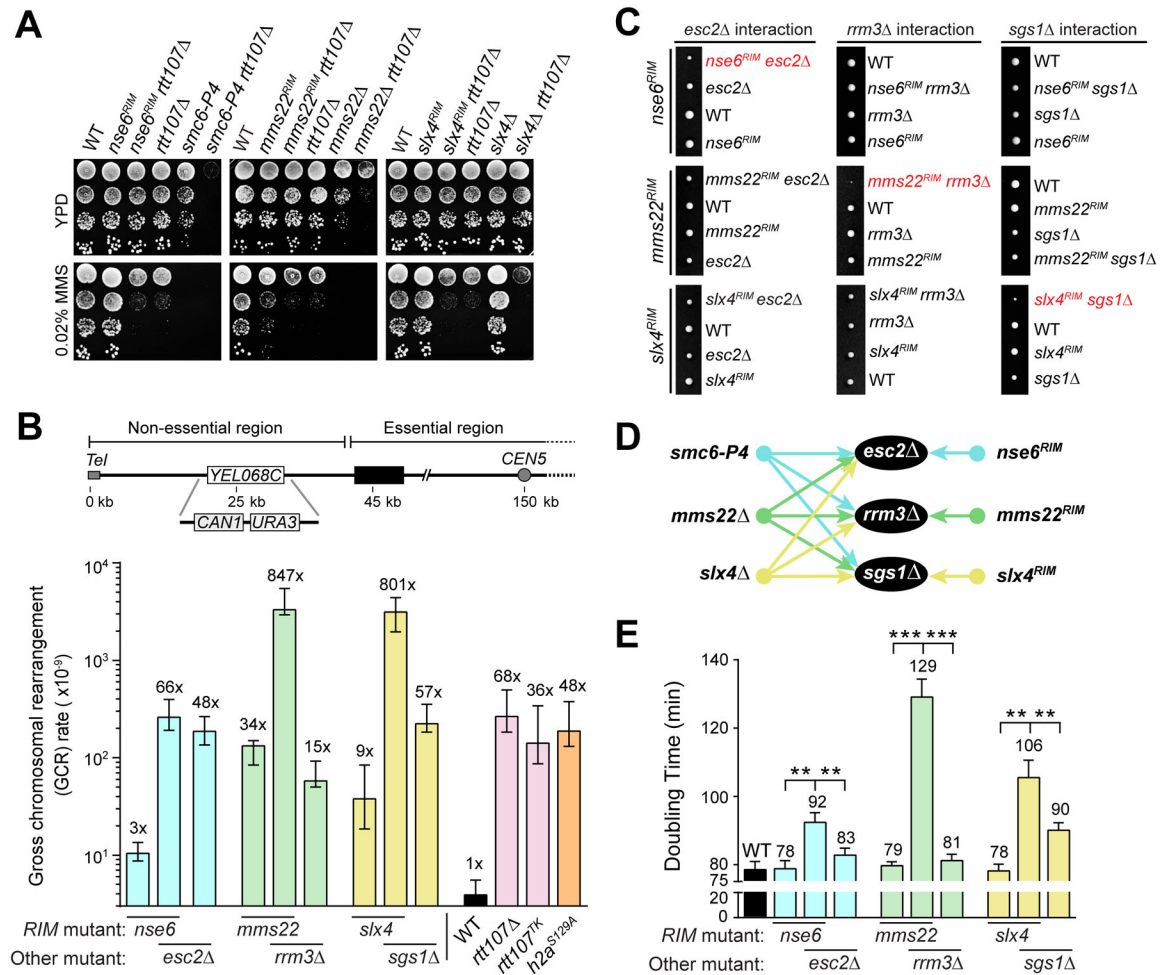
See also Figure S2, S3, S4 and S5.

Figure 5. Rtt107 binding of partner proteins promotes genomic stability during normal growth.
(A) The *RIM* mutants of *nse6*, *mms22*, and *slx4*, unlike their null or hypomorphic mutants, are epistatic with *rtt107* during growth (YPD) and under damage conditions (MMS, methyl methanesulfonate). Cells were spotted in 10-fold serial dilutions.

(B) The *RIM* mutants, *rtt107* mutants, and *h2a^{S129A}* cells exhibit elevated GCR rates. For each genotype, median rate of at least nine cultures was calculated from two biological duplicates. Error bars are the 95% confidence intervals. Schematic of the GCR assay is shown in the top panel.

(C) Representative tetrads of diploids heterozygous for indicated mutations. Negative genetic interactions are colored red.

(D) Summary of the genetic interactions of *RIM* mutants and their corresponding null or hypomorphic alleles with tester strains. Arrows indicate synthetically sick or lethal interactions.

(E) Cell doubling time measurement confirmed the negative genetic interactions between specific *RIM* mutants and deletions of distinct buffering genes. Three biological duplicates were used for calculation. Averages and standard deviations are shown; p-values are <0.01 (**) or <0.001 (***).
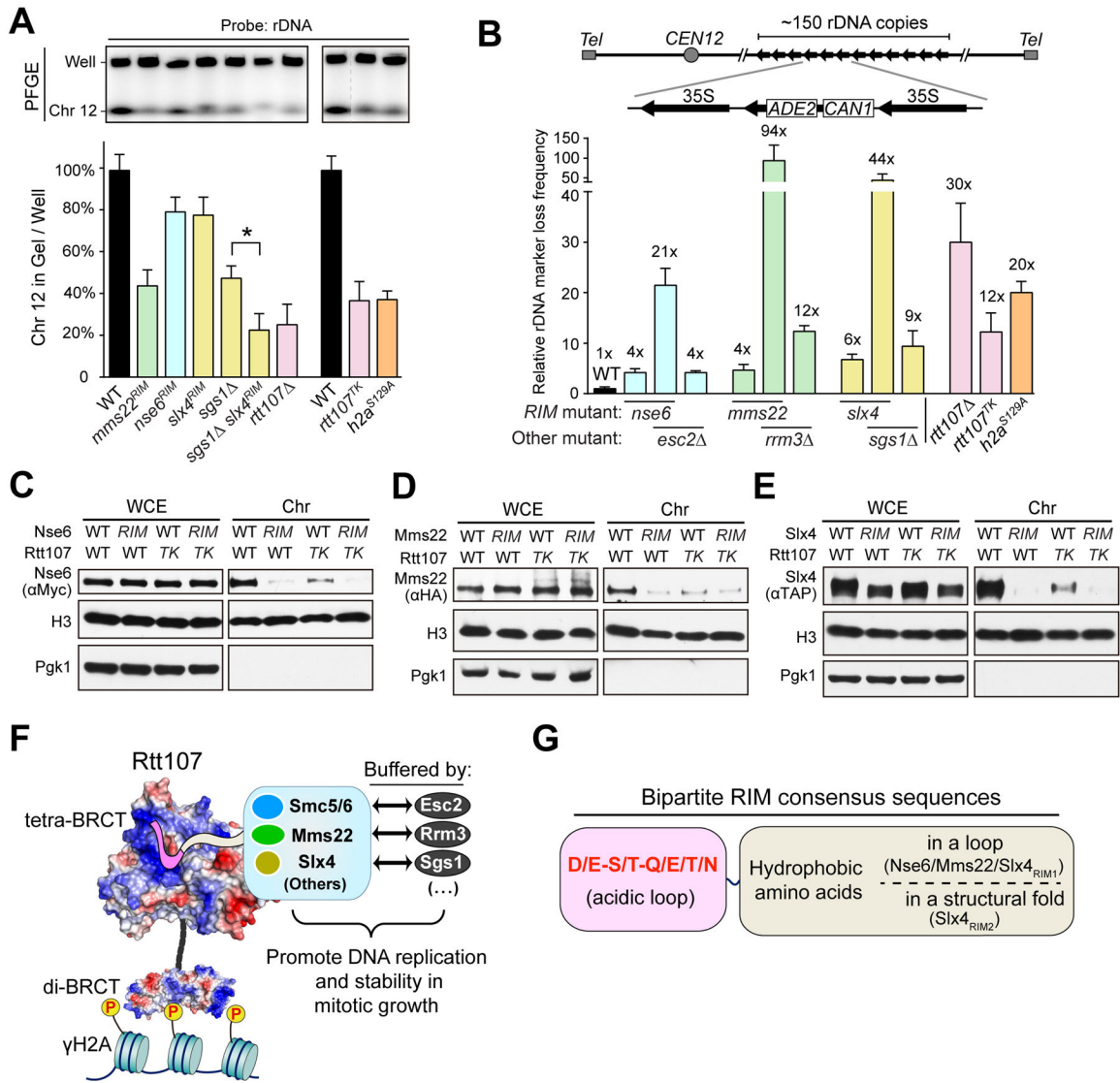
See also Figure S6.

Figure 6. Rtt107 targets partner proteins to chromatin to promote genome stability during growth.

(A) Examination of chromosome 12 replication. Southern blots were quantified to derive chromosome signals in gel versus well. Values were normalized to wild-type. Averages and standard deviations of two biological duplicates are indicated. Differences between mutants and wild-type, as well as between the two indicated mutants, were statistically significant ($p < 0.05$).

(B) rDNA marker loss rate measurement. Top: schematic of rDNA marker loss assay as described previously (Fritze et al., 1997). Bottom: averages of marker loss rates and standard deviations were calculated from three biological duplicates.

(C-E) Chromatin association of Rtt107 partner proteins. Whole cell extract (WCE) and chromatin fraction (Chr) were examined by Western blotting. H3 and Pgk1 are as markers for chromatin and non-chromatin fractions, respectively.

(F) A structural and functional model for Rtt107 control of diverse genome factors and pathways. Protein modification functions of Rtt107 partner proteins are highlighted: 'Su':

the SUMO E3 function of the Smc5/6 complex, 'Ub': ubiquitin E3 function of the Mms22 Cul8 complex, and 'P': a role of Slx4 in dampening checkpoint kinase phosphorylation. **(G)** Bipartite Rtt107 tetra-BRCT interaction consensus sequences derived from this study. See also Figure S7.

Table 1.

Crystal data collection and refinement statistics.

	Rtt107$_{NTD}$ (Hg-SAD)	Rtt107$_{NTD}$ (Native)	Rtt107$_{NTD}$-Nse6$_{RIM}$	Rtt107$_{NTD}$_Mms22$_{RIM}$	Rtt107$_{NTD}$_Slx4$_{RIM2}$
Data collection					
Space group	P2$_1$	P2$_1$	P2$_1$	P2$_1$	P1
Cell dimensions					
a, b, c (Å)	58.8, 152.9, 76.6	72.4, 98.9, 87.5	71.8, 101.4, 86.6	72.3, 99.7, 167.1	63.5, 78.0, 78.4
α, β, γ (°)	90.0, 106.9, 90.0	90.0, 109.0, 84.0	90.0, 108.6, 90.0	90.0, 94.9, 90.0	90.0, 79.2, 84.0
Resolution (Å)	2.8	2.3	2.4	2.3	1.8
R_{merge}	0.085 (0.406)[a]	0.070 (1.130)[a]	0.086 (0.484)[a]	0.085 (0.982)[a]	0.046 (0.672)[a]
$I/\sigma I$	11.0 (3.3)[a]	13.3 (1.0)[a]	12.1 (3.1)[a]	21.3 (2.0)[a]	15.0 (2.1)[a]
Completeness (%)	98.3 (99.8)[a]	97.7 (91.0)[a]	99.7 (99.9)[a]	99.1 (97.1)[a]	97.6 (96.1)[a]
Redundancy	3.8 (3.8)[a]	3.7 (3.1)[a]	3.8 (3.8)[a]	3.9 (2.2)[a]	3.9 (4.0)[a]
Refinement					
Resolution (Å)		49.45-2.31	45.71-2.40	49.43-2.30	35.87-1.80
No. of reflections		49,669	45,851	102,648	132,650
R_{work} R_{free} (%)		21.5/26.6	21.8/27.1	20.4/23.9	15.9/18.5
B-factors					
Rtt107$_{NTD}$		71.9	47.4	45.0	39.3
RIM		–	79.2	58.3	44.0
Water		64.7	33.9	37.7	44.8
R.m.s. deviations					
Bond lengths (Å)		0.008	0.009	0.009	0.006
Bond angles (°)		0.942	1.052	1.168	0.809
Ramanchandran plot					
Favored region		96.0%	95.2%	97.2%	98.5%
Allowed region		100.0%	100.0%	100.0%	100.0%
Outlier region		0.0%	0.0%	0.0%	0.0%

[a] Highest resolution shell is shown in parenthesis

KEY RESOURCES TABLE

REAGENT or RESOURCE	SOURCE	IDENTIFIER
Antibodies		
Anti-HA mouse monoclonal IgG2a (Clone: F-7)	Santa Cruz Biotech	Cat# sc-7392, RRID: AB_627809
Anti-Myc mouse monoclonal IgG1 (Clone: 9E10)	Bio X Cell	Cat# BE0238, RRID: AB_2687720
Anti-Flag mouse monoclonal IgG1 (Clone: M2)	Sigma-Aldrich	Cat# F1804, RRID: AB_262044
Anti-TAP rabbit antibody	Sigma-Aldrich	Cat# P1291, RRID: AB_1079562
Anti-Pgk1 mouse monoclonal IgG1 (Clone: 22C5D8)	Invitrogen	Cat# 459250, RRID: AB_2532235
Anti-Histone H3 rabbit antibody	Abcam	Cat# ab46765, RRID: AB_880439
Anti-mouse HRP-linked antibody	GE Healthcare	Cat# NA 931V, RRID: AB_772210
Anti-rabbit HRP-linked antibody	GE Healthcare	Cat# NA 934V, RRID: AB_772206
Bacterial Strains		
TOP10 Chemically Competent Cells	Invitrogen	Cat# C4040-10
BL21(DE3) Competent Cells - Novagen	EMD Millipore	Cat# 69450-4
Chemicals, Peptides, and Recombinant Proteins		
2-nitrophenyl β-D-galactopyranoside (ONPG)	Sigma-Aldrich	Cat# N1127-5G
ULP1 Protease	Home-made	N/A
PreScission (3C) Protease	GE Healthcare	Cat# 27084301
Deposited Data		
Structure of Rtt107$_{NTD}$ (tetra-BRCT)	This paper	PDB: 6J0V
Structure of Rtt107$_{NTD}$-Nse6$_{RIM}$	This paper	PDB: 6J0W
Structure of Rtt107$_{NTD}$-Mms22$_{RIM}$	This paper	PDB: 6J0X
Structure of Rtt107$_{NTD}$-Slx4$_{RIM2}$	This paper	PDB: 6J0Y
Mendeley Dataset	This paper	http://dx.doi.org/null/bj532s6vd4.1
Recombinant DNA		
pRS315-YEL072W:: URA3/CAN1 (for W303 GCR strain)	R. Kolodner	pRDK1378
pRS315-YEL068C:: URA3/CAN1 (for W303 GCR strain)	R. Kolodner	pRDK1379
pFA6a-4GS-6HA::NAT (for yeast gene tagging PCR)	This paper	pXZ1043
pBTM116-Rtt107$_{NTD}$ (2-513a.a.)	This paper	pXZ991
pGADT7-Nse6-FL	Zhao Lab	pXZ459
pACT2-Nse6$_{RIM}$ (2-46 a.a.)	This paper	pXZ990
pACT2-Mms22-FL	This paper	pXZ987
pACT2-Mms22$_{RIM}$ (2-38 a.a.)	This paper	pXZ986
pGADT7-Slx4-FL	Zhao Lab	pXZ458
pACT2-Slx4$_{RIM1}$ (407-445 a.a.)	This paper	pXZ989
pACT2-Slx4$_{RIM2}$ (535-587 a.a.)	This paper	pXZ988
pACT2-Scm3-FL	This paper	pXZ985
pACT2-Scm3$_{RIM}$ (165-223 a.a.)	This paper	pXZ984
pACT2-Rad55$_{RIM}$ (371-406 a.a.)	This paper	pXZ983
pACT2-Cdc7-FL	This paper	pXZ981
pACT2-Cdc7$_{RIM}$ (470-507 a.a.)	This paper	pXZ982

REAGENT or RESOURCE	SOURCE	IDENTIFIER
pGEX-6P-1-Rtt107$_{NTD}$ (codon-optimized Rtt107$_{2\text{-}513}$)	This paper	pXZ968
pGEX-6P-1-Nse6$_{RIM}$ (for peptide expression in *E. coli*)	This paper	pXZ967
pET28a-6His-Sumo-Mms22$_{RIM}$ (expression in *E. coli*)	This paper	pXZ966
pET28a-6His-Sumo-Slx4$_{RIM1}$	This paper	pXZ965
pGEX-6P-1-Slx4$_{RIM1}$	This paper	pXZ960
pGEX-6P-1-Slx4$_{RIM2}$	This paper	pXZ964
pGEX-6P-1- Scm3$_{RIM}$	This paper	pXZ963
pGEX-6P-1- Rad55$_{RIM}$	This paper	pXZ962
pGEX-6P-1- Cdc7$_{RIM}$	This paper	pXZ961
Experimental Models		
Organisms/Strains (*S. cerevisiae*/W303)	See Table S1	
Oligonucleotides		
Nse6^{RIM}-mut-FP: GAAACTGTACCAGCCGCGGCGATTTCAGGGTTTG	IDT	N/A
Slx4^{RIM1}-mut-FP: CTATTGTCTCAGATGCGGCTGATGAGACATCCAC	IDT	N/A
Slx4^{RIM2}-mut-FP: GTTGAGGCAAATGATGCGGAAGAAGAGGAGACA	IDT	N/A
Mms22^{D13A}-mut-FP: GTGATATCAGCGTCTGAGGCCACTG	IDT	N/A
Mms22^{Y33A}-mut-FP: CGAATTCAATGAAAATGCTTTATGGGCAGAGG	IDT	N/A
Software and Algorithms		
HKL3000	Minor	https://www.hkl-xray.com
Phenix	Adams	https://www.phenix-online.org
Coot	Emsley	https://www2.mrc-lmb.cam.ac.uk/Personal/pemsley/coot/
PyMOL	Schrodinger, LLC	https://pymol.org/2/
Origin 7	OriginLab	N/A
ImageJ	ImageJ software	N/A
GraphPad Prism 7	GraphPad Software	N/A
Others		
Ni-NTA Agarose	QIAGEN	Cat# 30230
Glutathione Sepharose 4B beads	GE Healthcare	Cat# 17-0756-05